University of Padova

Department of Physics and Astronomy "Galileo Galilei" - DFA

Master Thesis in Astrophysics and Cosmology

Star Formation at the Edge of Galaxies

Supervisor
Prof. Mauro D'onofrio
University of Padova

Co-supervisor
Prof. Ignacio Trujillo
Instituto de Astrofisica de Canarias

Master Candidate
Ouldouz Kaboud

Student ID
2071455

Academic Year
2023-2024

Contents

Abstract

At the edge of galaxies, in the lowest surface brightness regimes, lies the boundary where gas can collapse to form new stars. These regions remain largely unexplored due to the lack of very deep images that allow us to characterise the star-forming clumps at the edge of the discs. In this sense, we do not know whether stellar activity in these very low-density regions is similar to that in the more central regions of galaxies. To answer this question, we use the ultra-deep (limiting surface brightness 31 mag/arcsec^2) images of the LIGHTS survey obtained with the LBT in g and r bands, and the very deep Hα data obtained with the INT telescope. In this research, we will show for the first time how different the distribution of shapes and fluxes of star-forming regions at the edges of galaxies is compared to the active zones in the central parts of galaxies. We will discuss the implications of this discovery for understanding the current rate at which galaxy discs are growing.

Chapter 1

Introduction

For a comprehensive understanding of the structure and history of the Universe, it is essential to understand the formation and evolution of galaxies and for this, we need to dig deeper than just the bright central regions, exploring the faint outskirts as well, which are crucial to understand the ongoing star formation and disc growth. These low surface brightness edges shed light on what govern the gas dynamics and the conditions for star formation in less dense environments.
This study aims to address some of these fundamental questions by examining the star-forming regions of two galaxy disc galaxies using ultra-deep imaging.
In order to put the work done here in the right scientific context we give here a short discussion on the current theoretical ideas we have today on galaxy formation and evolution, discussing in the sections below the ΛCDM model (section1.1), the galaxy formation scenario (section1.2), and the current ideas about star formation and the dust roles in this regard (section1.3).

1.1 Lambda CDM Model

In recent decades, extensive studies have been conducted on the formation, evolution, and interaction of galaxies contributing to our understanding of the Universe. Among these, the most commonly accepted understanding of galaxy formation to date is based on the ΛCDM model. Modern cosmology is based upon the cosmological principle, the hypothesis that the universe is spatially homogeneous and isotropic, and Einstein's theory of general relativity, according to which the structure of space-time is determined by the mass distribution in the Universe. In combination, these two assumptions produce a cosmology (the standard model) which describes the change of the scale factor of the universe over time.
There are three main components of the universe as currently proposed by popular cosmologies. Aside from "baryonic" matter, such as protons, neutrons and electrons that make up the visible universe, astronomers have found evidence for dark matter and dark energy as well. Even though dark matter and dark energy are still unknown, we believe that they account for more than 95% of the universe's energy density.
Cosmological models differ mainly in (i) the relative contributions of baryonic matter, dark matter, and dark energy, and (ii) their nature.
The ΛCDM model is one of the most popular models, which is a flat universe in which about 75% of the energy density is attributed to a cosmological constant, $\sim 21\%$ to cold dark matter (CDM), and 4% to baryonic matter that forms stars and galaxies Houjun Mo and White (2010).
The Standard Cosmological Model states the following: the Universe began with the Big Bang,

went through a period of near-exponential inflation at early times ($\sim 10^{-35}s$), and has expanded ever since, under gravitational influence described by General Relativity. The expansion rate is governed by its contents, which are baryonic matter (and electrons) with density parameter $\Omega_b \simeq 0.04$, photons at 2.73 K and neutrinos (with negligible energy density), cold Dark Matter with $\Omega_m \simeq 0.26$ (0.22 in CDM), and Dark Energy, with $\Omega_{DE} \simeq 0.74$. Present-day Hubble parameters describe the expansion rate as $H_0 \equiv 100h \simeq 72$ kms^{-1}Mpc^{-1}. There are a few percent errors in these quantities. Despite the fact that it is spatially flat, or very nearly flat, it has evolved from adiabatic fluctuations and a near-scale-invariant spectrum, which is derived from primordial power spectrum, $P(k) \propto k^n$ with $n \simeq 1$, which was generated during inflation. Currently, the amplitude of fluctuations is measured by $\sigma_8 \simeq 0.75$ and the optical depth by $\tau \simeq 0.08$. A flat model with 6 free parameters $(\Omega_m h^2, \Omega_B h^2, h, n, \tau, \sigma_8)$ matches most observations, but there are extensions, where n varies with scale, or the mass of neutrinos is significantly different from zero. Nearly all cosmological observables are explained by this relatively simple model, including geometric measurements of the Universe, fluctuations, and light element abundances resulting from primordial nucleosynthesis. The Dark Energy in the simplest model is simply Einstein's cosmological constant Lambda(Λ) (Heavens (2008)).

1.2 The Galaxy Formation model

The study of galaxies and their formation is an important part of the cosmological scenario, providing insights into the mechanisms that govern the universe's large-scale structure and link the evolution of matter from its origins in cosmic fluctuations to the diverse array of galaxies we observe today. Our most accepted theory of galaxy formation to date is based on the ΛCDM theoretical paradigm. There is a full detailed description of galaxy formation and evolution in various textbooks (e.g., Houjun Mo and White (2010) and Baumann (2022)) that I will provide a brief synopsis of it here.

Perfect uniformity and isotropy of matter would not result in structure formation and some deviation from perfect uniformity is needed to explain presence of structure, in particular galaxies. Cosmic perturbations cannot be explained by the Standard Cosmology and it faces issues when applied to the early universe. It is necessary to extend the standard cosmology to include quantum processes in order to resolve these problems. A main consequence of this extension is the generation of density perturbations by quantum fluctuations at early times, which eventually led to the formation of the structures we see in the universe today.

The inflationary theory is one of the most successful extensions of standard cosmology, which assumes the Universe went through a phase of rapid, exponential expansion (called inflation) due to the vacuum energy of one or more quantum fields. There are some of these models that produce density perturbations with properties consistent with large scale structures. This implies that inflation can explain the physical reasons behind the initial perturbations.

After the initial perturbations, small differences in density begin to grow as a result of gravity. In fact, over-dense regions pull matter towards them and become even more over-dense and under-dense regions become even more rarefied as matter flows away from them. This amplification of density perturbations is referred to as gravitational instability. As density perturbations grow and collapse, they form nonlinear, quasi-equilibrium dark matter objects called dark matter halos, which are crucial to the formation of galaxies.

The widely accepted CDM model includes dark matter and regular matter (like gas), so each initial disturbance in the universe's density contains dark matter and baryonic gas in roughly their

universal proportions. As an object collapses, while the dark matter form a dark matter halo, the gas shocks to the virial temperature.
On the other hand, in the formation of galaxies, the cooling plays an important role. Different cooling processes can affect gas depending on its density and temperature. This cooling causes the baryonic matter to segregate from the dark matter, and accumulate as dense, cold gas in a protogalaxy at the center of the dark matter halo. As the consequence, the gas in a dark matter halo undergoes self-gravity dominating over the gravity of the dark matter causing it to collapse under its own gravity. Collapse increases the density and temperature of the gas, and this may eventually form stars, thus giving rise to a visible galaxy.
The first galaxies started to appear nearly a billion years after the Big Bang. There are about 100 billion galaxies in the observable universe, each with about 100 billion stars. There is an arrangement of more than 50 galaxies called "Local Group" that are gravitationally bound together and span about 10 million light-years. On even larger scales these galaxies formed clusters and superclusters over time with filamentary structures and giant voids in between them, a process which is still ongoing today. In the present-day Universe, a large percentage of galaxies are organized into groups and clusters that are the densest and most populous aggregations. In spite of the gravitational attraction between the clusters within the superclusters, they are spreading apart with the expansion of the universe. The largest such structures, like our Local Supercluster (de Vaucouleurs (1961)), are about 500 million light-years across. In fact, our Local Supercluster (LSC) is a planar structure across the sky formed by a thousand bright galaxies with apparent magnitudes $m_B < 13^m$ (Sandage and Tammann (1981)).
The galaxies studied in this research are NGC3486 and NGC2712. Both are members of the Local Group, dominated by the Milky Way and the Andromeda galaxy. With the deep images provided by the LIGHTS survey we would like to address here the problem of the star formation in galaxies. The survey LIGHTS will be discussed in Chapter 2.

1.3 The current ideas on Star Formation

The evolution of a galaxy is governed by the laws of structure formation in the universe. In particular, ΛCDM models support the theory that galaxies form from the inside out, meaning that young, metal-poor stars are found more near the edges of stellar discs than they are toward the center (Aumer et al. (2013); Abadi et al. (2003)).
Conversely, El-Badry et al. (2016)'s studies and explorations of stellar feedback revealed outflows of significant gas mass beyond the stellar radius that they cool and fall back into the galaxy center on timescales of a few 100 Myr. Through their evolutionary histories, these outflow and in-fall cycles have driven strong fluctuations in galactic potential, leading to dramatic effects on stellar populations. A main result of this phenomenon is that stellar migration can systematically change radial gradients of stellar age and metallicity because the amount of outward migration depends on stellar age. So, current population gradients may not reflect intrinsic gradients at formation, and radial SFHs inferred from present-day population gradients, as often done in galactic-archaeology studies, are likely to be severely biased.
In addition to the stellar disc, the stellar halo can also be modeled as a result of major and minor mergers and accretions. For instance, based on the study done by Alberts et al. (2011), the outer disks of galaxies are mainly about 100 million years old, ranging from 1 million to 1 billion. This explains why there are fewer Hα emissions in these regions as Hα can only be observed in star-forming regions younger than 10 Myr as sign of young stars.

The stellar halo can also be explained by the phenomenon of stellar migration (Sellwood and Binney (2002)). Stars and gas in galaxy discs are churned by spiral waves in a manner that preserves their angular momentum distribution and causes little random motion to occur. Over the lifetime of a disc, individual stars' angular momenta can change by up to 50%. In an individual spiral wave, changes are concentrated around its corotation radius; however, since transient waves develop rapidly, changes affect the entire disc. Because the interstellar medium is also stirred by this mechanism, it has profound consequences for the metallicity gradients with radius in both stars and gas. In both scenarios, the stellar halo build-up was simulated as a result of past mergers and accretion events or as a result of stars migrating, allowing older populations to populate edges of galaxies.

In our case, we examined the star formation activities in galaxies belonging to the Local Group using extensive data from the LIGHTS survey. Using these data, we can gain valuable insight into the evolution of galaxies.

"Star formation laws" describe empirical relationships between interstellar gas and the star formation rate (SFR) of it. In both nearby and far galaxies, these relationships arise as a result of the physical processes that govern star formation (SF) in the interstellar medium (ISM) (review of Kennicutt and Evans (2012)).

Since the pioneering work of Schmidt on 1959 (Schmidt (1959a)), many forms of SF laws have been proposed in the literature. Star formation laws fall into two main categories, "integrated" and "resolved". The "integrated" SF laws connect unresolved, global measurements of galaxy gas mass and SFR (e.g., Saintonge et al. (2011), Kennicutt (1989), de los Reyes and Kennicutt (2019)). The "resolved" SF laws on the other hand, elate the local surface densities of gas mass and SFR (e.g., Wong and Blitz (2002), Bigiel et al. (2008)) There have been alternative formulations that have modified the basic relationship by, for example:

(a) The ones that as opposed to the total neutral gas, only taking into account molecular gas (e.g., Wong and Blitz (2002), Bigiel et al. (2011)) or dense molecular gas (e.g., Gao and Solomon (2004), Lada et al. (2012))

(b) Those that consider volume densities instead of surface densities (e.g., Schmidt (1959b), Bacchini et al. (2019))

(c) Including additional information beyond gas mass/density for the independent variable, such as orbital time (Elmegreen (1997)).

At least four of the resolved SF laws have received greater attention in recent years.

(1) The molecular Kennicutt–Schmidt (mKS) relation (Kennicutt Jr (1998)) between the surface densities of molecular gas and SFR.

(2) The molecular Elmegreen–Silk (mES) relation (Elmegreen (1997)) between the SFR surface density and molecular gas surface density divided by orbital time;

(3) The free fall time-regulated SF relation (FFTR relation; McKee and Ostriker (2007); Krumholz et al. (2011)) linking the SFR surface density to the molecular gas surface density divided by the molecular cloud free fall time;

(4) The pressure-regulated SF relation (PR relation; Ostriker and Shetty (2011)) connecting the SFR surface density to the ISM dynamical equilibrium pressure.

Alternatively, the nebular Hα recombination line and the ultraviolet (UV) continuum are two of the most widely used tracers of recent star formation. The Hα is the result of recombination of gas ionized by photons from massive stars ($\geq 15\,M_{\odot}$), and is expected to occur over the lifetimes of extremely massive stars (≤ 5 Myr), while the UV continuum is caused by non-ionizing photospheric emission from stars with $M \geq 3\,M_{\odot}$. These two integrated tracers provide insight into current and recent star formation in nearby and distant galaxies (Weisz et al. (2012)). Hα emission has

also been identified by many researchers as one of the most effective tracers of young stars (within the last 10 million years) (Haydon et al. (2020); Shivaei et al. (2015)) which we will also use as a method in our analysis for detecting star forming regions.

1.3.1 The role of dust on star formation

Star formation rate (SFR) of galaxies is fundamental in understanding their star formation histories (SFHs) over cosmic times (Madau and Dickinson (2014)). There is a strong link between interstellar dust and star formation activity in galaxies as well. Dust grains condense in the cold envelopes of evolved stars and in supernova ejects. In return, they promote molecular hydrogen formation, shield the molecules from ultraviolet radiation, and contribute to the formation and cooling of molecular clouds which collapse to form a new star (da Cunha et al. (2010)). Studies done by Lianou et al. (2019) revealed that the dust mass (M_{dust}) in a galaxy is linked to the star formation rate (SFR), showing that star formation efficiency in relation to dust (SFR/M_{dust}) is nearly constant regardless of galaxy types.
Additionally, dust is responsible for shaping the spectra of galaxies, as it attenuates radiation at short wavelengths and radiates energy in the infrared region (Draine (2003)). Approximately 30% or more of the energy emitted as starlight in the Universe is reradiated by dust in the infrared spectrum (Bernstein et al. (2002)). Moreover, interstellar dust determines how galaxies look, how the interstellar medium behaves, and how star formation takes place in a galaxy.
On the other hand, dust plays a crucial role in measuring star formation rates in galaxies. In fact, Buat (2002) studies highlights a strong correlation between H-alpha and UV emissions in nearby star-forming galaxies, and suggests that both emissions are affected by dust extinction. Therefore, understanding and correcting for dust extinction is essential for accurate estimation of star formation rates in galaxies.

This thesis would like to contribute to our understanding of the star formation problem inside galaxies. By exploiting the deep images obtained by the LIGHTS survey and the deep $H\alpha$ images obtained by the INT telescope, we want to discuss in particular the problem of the star formation in the outermost regions of galaxies.
This thesis is structured as follows: section2 contains the dataset used in this study, including details on the LIGHTS survey and the Isaac Newton Telescope (INT) as well. This section also includes few details about the target galaxies. In section3 we describe the methodology, including the observational strategy, data calibration, catalog-making process, and selection criteria for star-forming clumps. section4 discusses the results, focusing on the properties of star-forming clumps at different radial distances from the galaxy center and their implications for star formation. Lastly, section5 summarizes our findings and their significance for understanding galaxy disk evolution, as well as future research suggestions.

Chapter 2

Our Dataset

2.1 The LIGHTS Survey

The purpose of this chapter is to present the LIGHTS survey data that have been used in this study. LIGHTS (LBT Imaging of Galaxy Haloes and Tidal Structures) is an ongoing observational campaign with the 2×8.4, m Large Binocular Telescope (LBT) intended for the study of the stellar haloes and the low surface brightness population of satellites down to a depth of $\mu_V \sim 31$ mag arcsec^{-2} (3σ in $10'' \times 10''$ boxes) of nearby galaxies. The observations were performed using the Large Binocular Cameras (LBCs) of the LBT telescope in the Sloan g and r bands. Two major objectives of LIGHTS survey are to addressed a pair of problems that are closely relate to the nature of dark matter: the properties of stellar haloes of galaxies, and the population of faint satellites that surround them. In the paper published on 2021 Trujillo et al. (2021) showed that the ultra-deep imaging from LBT is capable of detecting satellites down to $M_V = -8.25$ mag and with central surface brightness of $\mu_g(0) = 27.1\,\mathrm{mag\,arcsec^{-2}}$ at a distance of 13.5 Mpc. When fainter systems are targeted, the contrast between them and the background galaxy population should increase not only as a result of targeting fainter systems, but also as a result of targeting low surface brightness objects and as a result of this potential improvement in determining which fraction of faint galaxies are real satellites, we may be able to extend our capability to investigate the 'missing satellites' problem beyond the Local Volume(i.e. at distances beyond 12 Mpc). Therefore, using ultra-deep imaging, this survey aims to systematically detect stellar haloes and 'missing satellites' galaxies (if any) of a representative sample of nearby ($D \sim 20$ Mpc) galaxies. As a result, they aim to achieve the most faint surface brightness limit possible while maintaining the highest degree of angular resolution for classifying and masking contaminating sources. In order to select targets, several criteria were used, including the ability to differentiate between extended stellar disks and halo components, and pragmatic ones, such as the view field of the camera Zaritsky et al. (2024). This selection are drawn from the Sienna Galaxy Catalog 2020 Moustakas et al. (2023). The following six selection criteria were used (with specific exceptions noted below):
(1) The declination of grater than $-10°$ in order to allow observation of relatively low air mass (air mass < 1.4) from the LBT which is at latitude $\sim 32°$;
(2) The angular diameter should lies between $4'$ and $10'$ as measured by D26, which corresponds to the r-band 26 mag arcsec$^-2$ isophote, in order to be in agreement with the field of view of the Large Binocular Cameras (LBC) instrument;
(3) The axis ratio, $\frac{b}{a}$, < 0.8 to highlight the geometric difference between a stellar halo and an extended disk component;
(4) The Galactic reddening, E(B - V), should be less than 0.04 as measured by Schlegel et al.

(1998) avoiding regions of high Galactic extinction;
(5) The redshift, z, should not exceed 0.006 (closer than $\sim$ 26Mpc) in order to limit the study to nearby galaxies and provide us with high physical resolution (corresponding to $\sim 30\,\mathrm{pc\,pixel}^{-1}$ at the native image resolution and $100\,\mathrm{pc\,pixel}^{-1}$ in the binned images we will use for detecting low surface brightness satellite candidates);
(6) an absence of nearby projected bright stars. First determination done using an automated pass through the Yale Bright Star Catalog to search for stars within 1° and then a visual examination based on experience as the program progressed).
Table 2.1 shows two of the LIGHTS target galaxies that have been utilized in our research with some of their properties. A complete list of these fields can be found in Table.1 of the article Zaritsky et al. (2024).

Name	R.A. (deg)	Decl. (deg)	m_g (mag)	m_r (mag)	D (Mpc)	b/a	Morph
NGC2712	134.87698	44.91390	12.33	11.62	30.2	0.54	SBb
NGC3486	165.09945	28.97514	11.00	10.42	13.6	0.87	Sc

Table 2.1: LIGHTS Target Galaxies

The published distances are based on studies utilizing standard candles (SNe, TRGB, and Cepheids), scaling relations (Tully-Fisher), and detailed cosmological flow models. In general, distance measurements are employed based upon the assessment of their relative merits.
The images of these two fields called NGC 2712 and NGC 3486 is shown in Fig. 2.1 and Fig. 2.2 respectively.

There are instances in which the selection criteria have been violated. For instance, the D26 criterion can be exceeded by including NGC 2903, NGC 5033, and NGC 5907, all of which have a D26 greater than 10′ (12.82, 11.53, and 21.16, respectively). Including NGC 1042, NGC 3351, NGC 3486 and NGC 3596 (0.87, 0.89, 0.87, and 0.91, respectively) also violate the $\frac{b}{a} < 0.8$ criterion. Having a shortage of more suitable targets, the remaining galaxies that violated the criteria and were not included in an earlier study have been included. According to Fig. 2.3, the sample contains galaxies that resemble the Milky Way morphologically but have a median magnitude of one mag smaller (-20.6). Overall, the sample cannot be regarded as Milky Way analogs, although a subsample of five galaxies (NGC 3675, NGC 3953, NGC 4321, NGC 5907, and NGC 5033) may qualify as such if a closer comparison is desired.

2.1.1 Large Binocular Telescope (LBT)

The Large Binocular Telescope (LBT) Observatory located at Mt. Graham in southeastern Arizona is a collaboration between institutions in Arizona, Germany, Italy, Indiana, Minnesota, Ohio and Virginia Hill et al. (2012). Using two 8.4 meter diameter borosilicate honeycomb primary mirrors mounted side-by-side, it produces an 11.8 meter circular aperture. LBT has the advantage of being able to produce phased-array imaging of an extended field by combining the light from the two primary mirrors. In combination with adaptive optics, the telescope has a diffraction-limited resolution of 22.65 meters.
There is a wide-field double imager instument named Large Binocular Camera (LBC Ragazzoni et al. (2000), Pedichini and Speziali (2004)) located at the prime focus of the twin 8.4 m Large

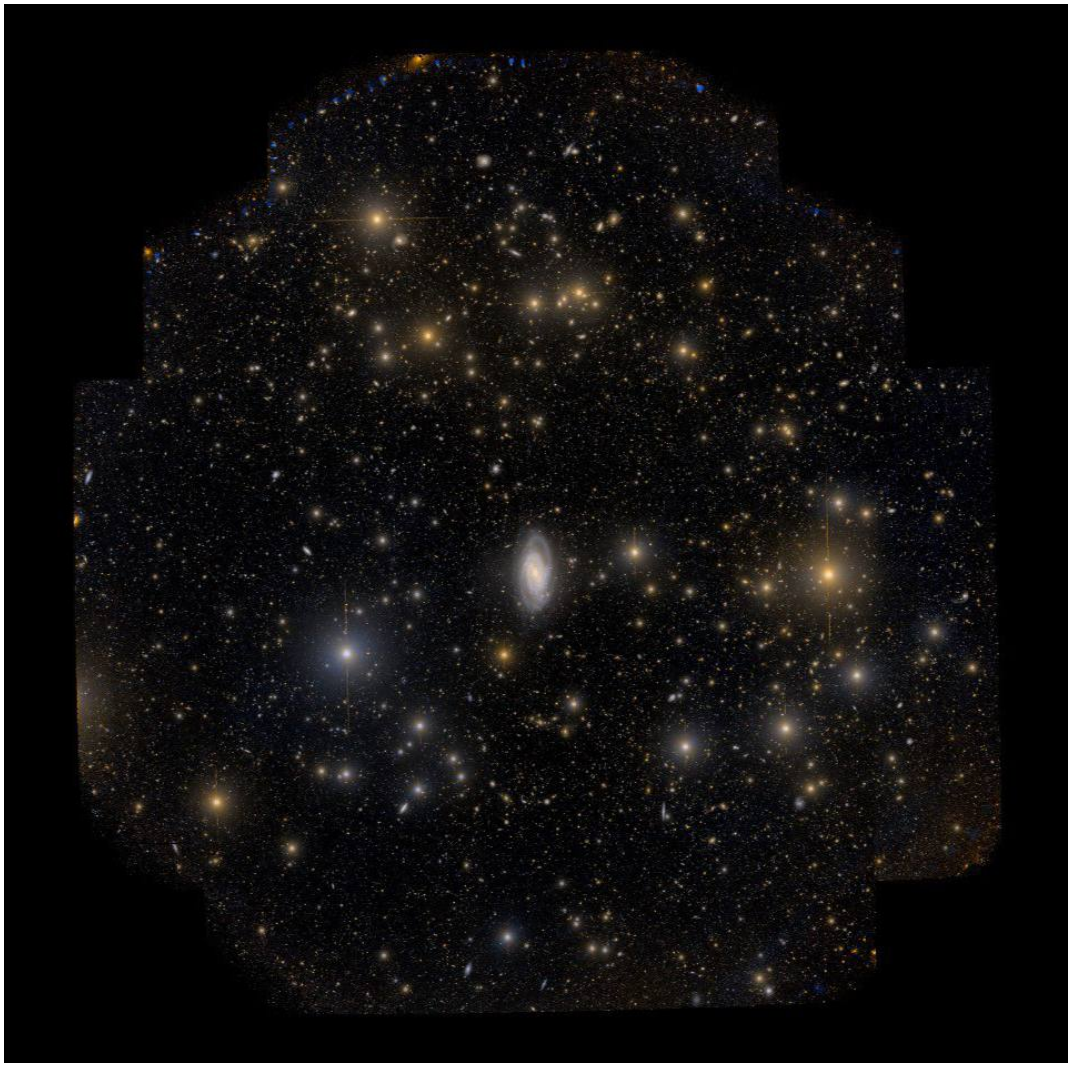

Figure 2.1: RGB image of NGC2712

Binocular Telescope (LBT). The two channels have been optimized for different wavelength ranges: the blue channel (LBC-Blue) is designed for the U, B, and V bands, and the red channel (LBC-Red) is designed for the V, R, I, and Z bands. With a focal ratio of F/1.45, deep imaging becomes possible over a field of view size of approximately 30 arcmin. Observing a given target simultaneously over a wide wavelength range is possible due to the mirrors of both channels mounting on the same pointing system. In each of the two LBC cameras, there are four CCDs, with a pixel scale of 0.224 pixel^{-1} , covering an approximate area of 7.8×17.6 per CCD, with $\sim 18''$ wide gaps between the chips.The combined field of view for each LBC camera is roughly $23' \times 25'$.
Ultra-deep observations of LIGHTS targets that have been used in our study, obtained using the LBT and both channels (blue and red) of the LBC simultaneously. From 2020 October through the first half of 2023, observation of this survay was carried out during Director Discretionary Time (DDT; P.I. D'Onofrio) and standard allocated time (P.I. Zaritsky). g-SLOAN filters were used on the LBC Blue camera and r-SLOAN filters on the LBC Red camera for wavelength ranges of 3500 Å $-$ 6500 Å and 5500 Å–1 μm, respectively. Under good seeing conditions, images have been taken, resulting in a full width at half maximum (FWHM) seeing of about 0.900 in both bands.

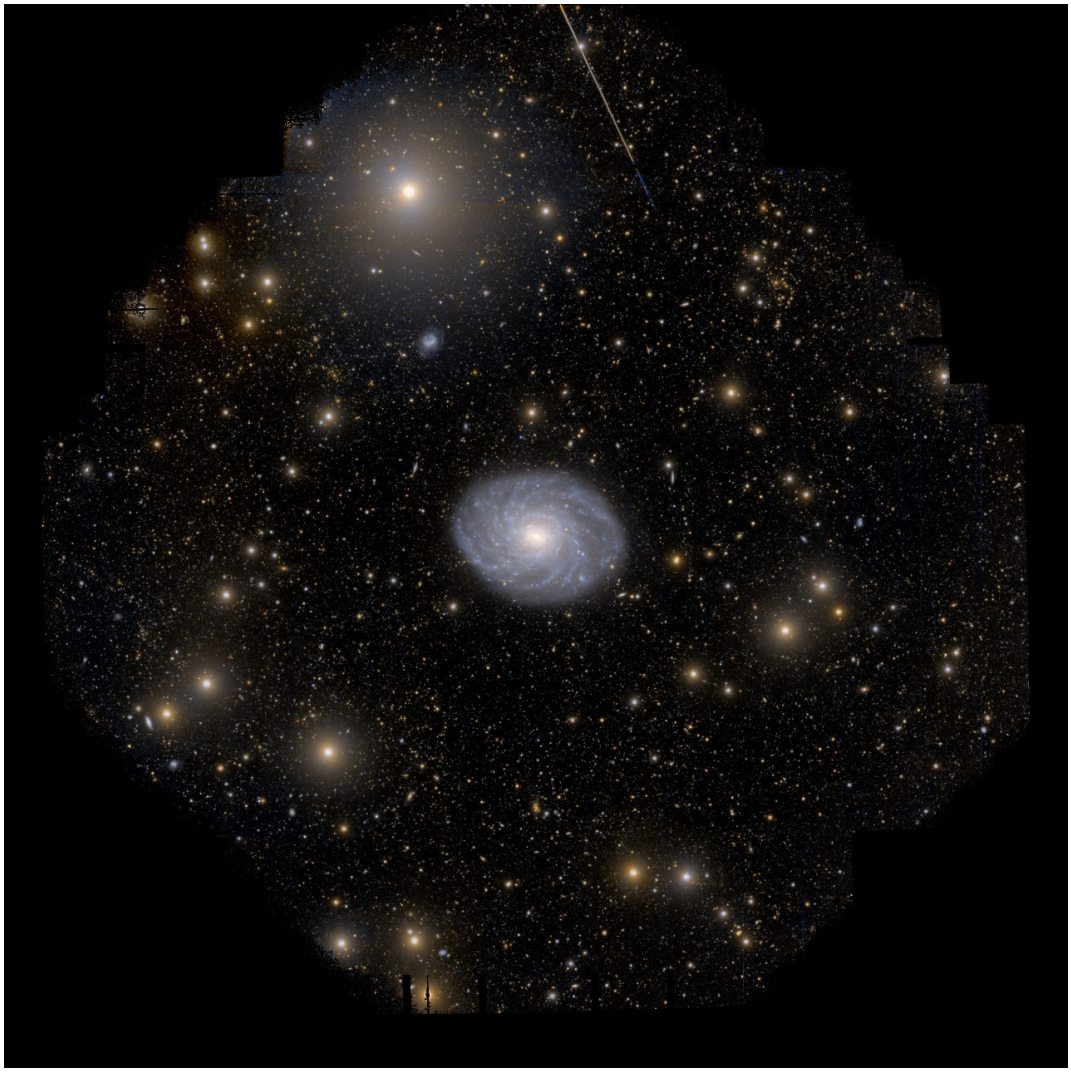

Figure 2.2: RGB image of NGC3486

2.2 Isaac Newton Telescope (INT)

For the collection of Hα data, The Isaac Newton Telescope (INT) have been utilized. A number of years after the INT began operations in Herstmonceux, United Kingdom, it became apparent that the telescope would perform better astronomically under better astronomical weather conditions. It was decided to move the telescope to La Palma in 1984, where it resumed operations after such conditions are found at the Roque de Los Muchachos Observatory.
There is a 2.5 metre primary mirror on the Isaac Newton Telescope with focal length of 7.475-m, giving a focal ratio of f/2.94 at the uncorrected primary focus. It uses an equatorial mount that is made of polar discs and forks. Instruments can be mounted at the prime focus or at the Cassegrain focus, and they are suitable for wide field imaging as well as intermediate and low dispersion spectroscopy. An advanced instrument, the Wide Field Camera has the ability to perform high resolution, very deep, wide field optical imaging surveys, using a CCD mosaic that covers approximately a half-degree circle of view, roughly equal to the size of the moon.
There have been a great deal of scientific highlights obtained with the Isaac Newton Telescope over the years. For example, it has contributed significantly to the study of quasars, supernovae,

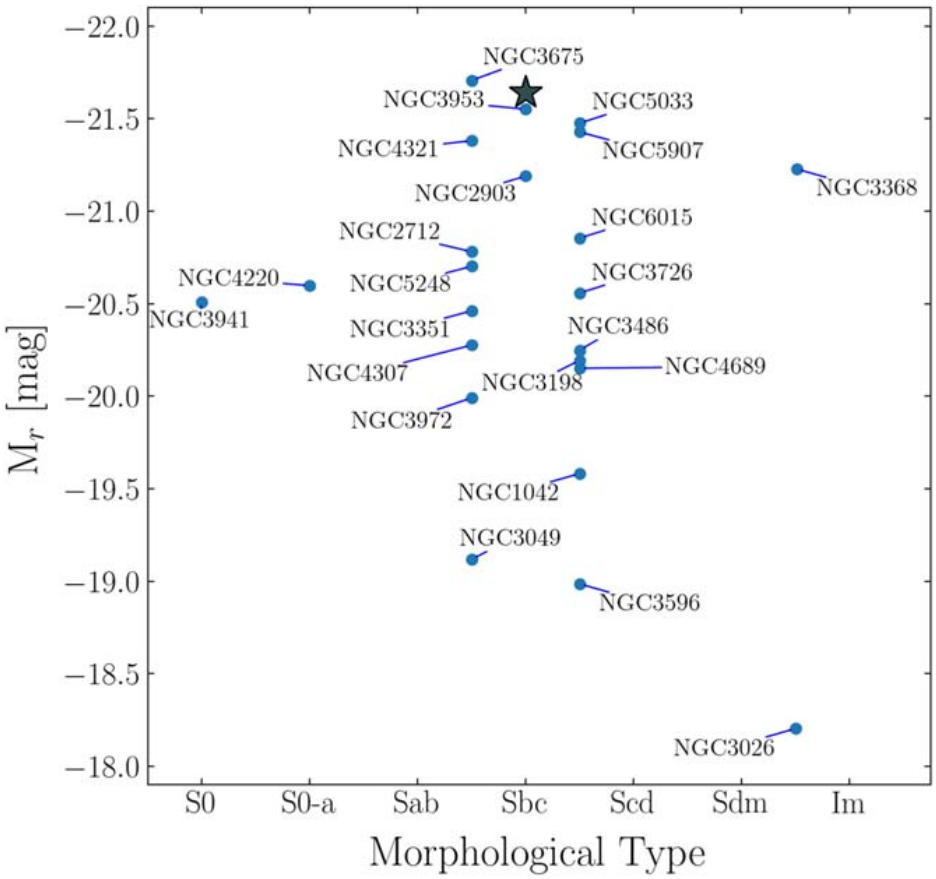

Figure 2.3: This is the LIGHTS sample to date in terms of morphology-absolute magnitude. For comparison, the Milky Way is represented by $Mr = -21.64$ Bland-Hawthorn and Gerhard (2016) and a morphological classification of Sbc (Hodge (1983); Kennicutt (2001).

black holes, dwarf galaxies, milky way galaxies, planetary nebulae, and stars evolution. Among the most outstanding results obtained with the Isaac Newton Telescope is the first observational evidence of black holes.
In comparison with its earlier incarnation at Herstmonceux, the new INT at La Palma differs significantly in mechanics, electronics, and optics:

- There has been a large change in angle to the polar disc resulting from the change in latitude from 50 degrees 51 minutes 58 seconds to 28 degrees 45 minutes 43.4 seconds.
- For operation at -30 degrees declination, a segment of the disc was removed.
- A new computer control system was written, along with new encoders and drive electronics.
- The mirror was resized to 100 inches from 98 inches, improving the optical quality significantly.
- As with the acquisition and guidance boxes at the Cassegrain focus, the old prime-focus assembly was completely replaced with a remote-controlled one.
- An entirely new dome houses the telescope, the old dome being left in place as a landmark for channel shipping.

- Finally, there are a number of new instruments, as well as a computer system that controls them.

Instruments available at the INT include a Wide Field Camera (WFC) and an Intermediate Dispersion Spectrograph (IDS):
(1) Wide Field Camera (WFC): Captures images over an area of 33 arcmin using a wide range of narrow-band and broad-band filters.
(2) Intermediate Dispersion Spectrograph (IDS): Long-slit spectroscopy with medium-low resolution. There are 16 gratings available with IDS, providing dispersions between 4.0 and 0.24 $\text{Å}\,\text{pixel}^{-1}$. Default detector is Red+2, but it can be substituted with EEV10 (if requested and justified in the proposal).
There may also be more detailed information regarding this telescope on INT's original website [1]. Using the INT telescope, we have collected $H\alpha$ data for two fields, NGC 2712 and NGC 3486, ranging between 6490 and 6646 Angstrom. We will describe its calibration and continuum removal in the following sections.

2.3 Target galaxies: NGC 2712, NGC 3486

It is clear that individual galaxies can reveal important information about their formation and evolution by understanding their characteristics and structures. therefore, our two target galaxies, NGC 2712 and NGC 3486 will be examined briefly in this section. Their morphological classifications and the implications for their stellar and gas distributions will be discussed shortly.
It was suggested by Shen and Zheng (2020) to classify NGC 3486 as Sc(r)I-II type which claims it to be a moderately structured spiral galaxy with a ring feature, characterized by its surface brightness and activity level in its central region.
On the other hand, near-IR images, NGC 2712 was suggested to be classified as a double-barred galaxy by Márquez et al. (1999). In reply, the William Herschel Telescope has provided higher resolution images of the inner elliptical feature which had been identified by M.arquez et al. to show that it is an irregular nuclear ring, and that there is no evidence for a bar inside the ring Erwin (2004).
The NGC 3486 galaxy is a low-luminosity active galaxy, with a black hole that is less bright at the center. In addition, Annuar et al. (2020) claims that it emits comparatively small amounts of X-rays, is not heavily obscured by gases or dust, and is not strongly suggested to have significant nuclear dust. However, studies by Foschini et al. (2002) using XMM-Newton telescope annonces for presence of six ultraluminous X-ray sources (ULXs) in four nearby galaxies, including NGC 3486.
On the other hand, regarding NGC 2712, N-body dynamical models suggest that the bar structures in galaxies like NGC 2712 are likely formed by gravitational instability and can last for a long time (Khoperskov et al. (2001)). Additionally, Huchtmeier and Richter (1985) 's research on hydrogen gas (HI) in three isolated galaxies, including NGC 2712, shows their hydrogen masses are higher than usual for their type. This claim strengthened by maps made with the Westerbork Synthesis Radio Telescope which showed HI emissions from the isolated galaxy NGC 2712 (Krumm and Shane (1982)). This study on the other hand, claimed that NGC 2712 does not have a larger hydrogen distribution compared to non-isolated galaxies, suggesting that the gravitational effects from other galaxies might not significantly influence its gas structure. Furthermore, it was

[1] `https://www.ing.iac.es/Astronomy/telescopes/int/`

discovered that twists and unevenness in the gas distribution within NGC 2712 could be the result of natural processes, not just interactions with other galaxies.

Chapter 3

Observations and data analysis

3.1 Observational strategy

LIGHTS Survey observation aimed to reach the theoretical surface brightness limit of the GTC (Gran Telescopio Canarias) in the allocated time (8.1 hours on source) Trujillo and Fliri (2016). The observational strategy has been designed so that the background around our galaxy target become as flat as possible to avoid several observational biases that may affect very deep observations, including fringing, scattered light, saturation, ghosts, etc. Therefore, in addition to conducting the usual dithering scheme, a rotation pattern have been pursued. The reason is to remove as far as possible effects due to contamination by scattered (residual) light. The rotation pattern eliminates the possibility of reflected residual light (from the telescope dome, telescope structure, etc.) that may have an effect on the camera during the full set of pointings at the same position angle (P.A.). Furthermore, the large number of images (243) made it possible to build a very flat sky.
This strategy composes of three steps which is carried out on the nine observing blocks:

- Step A: The camera's P.A. has been fixed at a given angle and a dithering pattern has been developed for nine positions.
- Step B: After rotating 120° the P.A., dithering patterns of nine positions have been repeated.
- Step C: The P.A. is rotated another 120° and the dithering pattern of nine positions is repeated.

If accuracy is to be achieved, it is necessary to follow a dithering pattern with a step size similar to or greater than the size of the main object under study Trujillo et al. (2021). Time was divided between 30 different pointings with 180 s exposures each for a total of two hours. In each filter, the total time spent on-source was 1.5 hours. For flat-field precision, contrary to the procedure described earlier, the camera has not been rotated but has used a single position angle for all exposures due to the relatively short amount of time spent on source.
This dithering pattern is illustrated in Fig. 3.1, which shows the weight maps (for the g and r bands) that were generated through the stacking of all the individual frames. According to the observation pattern, the galaxy is never located on the same physical area of the CCD during the 30-exposure period and also it eliminates gaps between the LBC CCDs.

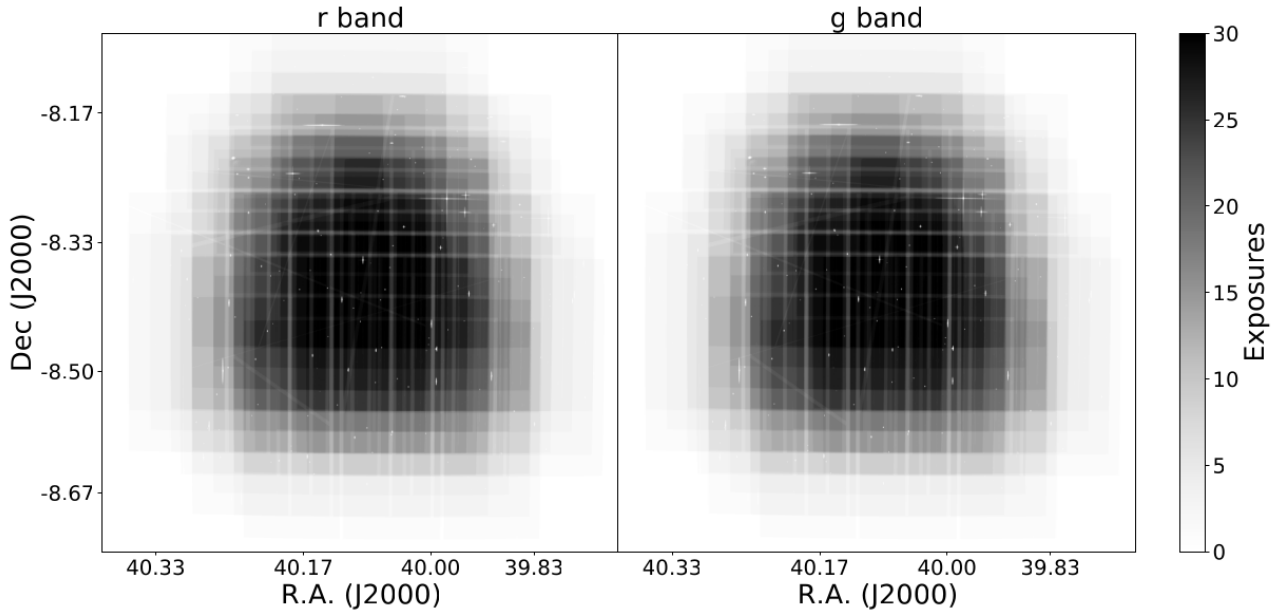

Figure 3.1: Sloan g- and r-band weight maps after stacking, which clearly indicate a dithering pattern in the present observation. A darker area indicates a greater number of repetitions and therefore a deeper image.

3.1.1 Flat-field Correction

Deep imaging requires precise flat-field correction. In the case of LBT, dome flats are unsuitable due to irregularities in the dome illumination Zaritsky et al. (2024). Furthermore, twilight flats are not fully useful due to variations in night-sky illumination and twilight light gradients from the horizon where the sun sets. Therefore, the master flat is created using our own set of science images in order to sidestep these issues. The complete set of science images would seem to produce a more high-quality master flat, but the variation in focus, vignetting, air mass, and moon illumination from night to night, as well as the scattered light from bright stars and light pollution from nearby populations, result in less than optimal flat-field frames. This problem was addressed by only using the data collected on each night to create the flat-field image for that night's data. The master flat for each night must be created with at least 15 science images. For statistical robustness, this minimum number is essential.

A bias-corrected science image has been generated for each night of observation, each filter, and each CCD.

There are two steps in this process:

The first step is to identify those CCD images that should be rejected due to the gross non-uniformity of the illumination on the large scale. There are variety of criteria that have been impose. For instance,the CCD images that contain a bright star (MV$<$ 9 mag) have been rejected or where the target galaxy covers 60% or more of the CCD have been excluded. It is also important to remove any CCD images from the stack in which there is a very small distance between the central pixel and the bright star (this distance varies depending on the brightness of the star being viewed, ranging from $7'$ to $5'$ for a bright star 5.5 magnitude and 8.5 magnitude). Those images in which the central pixel is either equal to or less than half of the semi-major axis of the target galaxy, were rejected as well. The percentage of images excluded per CCD varies according

to the specific field, ranging from 5 to 30 percent in both g and r filters. Dithering with large displacements ensures that each CCD receives enough frames that are free from the central galaxy. As next step, master flat has been created. The procedure of it described in detail in Trujillo and Fliri (2016):

- Using SExtractor Bertin and Arnouts (1996), an object mask has been created for each 120 s science image. Expanding the masks of objects ensures that the outer light of the objects is also masked. In order to create the final masterflat, only pixels outside the masks are used.
- Each science image of a given night is normalized to one. To normalize each image, the number of counts is determined at the same CCD position (close to the optical axis of the camera) within a box of $50 \times 50\,\mathrm{arcsec}^2$.
- By using the median, normalized and masked individual science images are combined into a single masterflat.

This method has yielded four preliminary masterflats, one for each CCD. Finally, bias-corrected science images are divided by their flat-field CCD counterparts. For the purposes of avoiding vignetted areas at the corners of the detectors, we remove from the image all pixels where the illumination fraction for the flat field image is < 0.9.

3.1.2 Sky background determination

The proper sky subtraction is essential when dealing with low surface brightness data, so as not to introduce artificial gradients and impact subtle structures Zaritsky et al. (2024). Sky levels in CCD images have been assumed to be approximated by constant values. The purpose of this is to prevent inadvertently modeling out physical low surface brightness features and expect the extensive dithering to mitigate spatial variations in the sky. A well-defined point-spread function has been used to address gradients caused by scattered light from bright stars. In NoiseChisel from Gnuastro, the `--checksky` option Akhlaghi (2019) has been used to compute the sky.
In fact, for each CCD, we calculate the median of the Sky image produced by NoiseChisel and we remove that value from the image Trujillo et al. (2021). It is done under very conservative conditions in order to avoid removing any potential large-scale low surface brightness feature that might be present in our data by avoiding polynomial fits. After masking bright sources and diffuse light that may cause biased background values and result in an over-subtraction, the sky value for each image has been determine by calculating the 3σ clipped median of the non-masked pixels. It ensures that a locally representative sky value for that region has been obtained by using CCD images covering an area of approximately $14' \times 8'$. As a final step, each CCD image taken during the observation night has been subtracted from the corresponding sky value Zaritsky et al. (2024).

After sky subtraction, LBT counts (ADUs) have been converted into nanomaggies [1]. This is accomplished by constructing a catalog of sources for each set of images that is common between SDSS and LBT images, cross-referencing with Gaia eDR3 to confirm the presence of point-like sources, and measuring flux within circular apertures with a diameter of $2''$ (for Gnuastro routines to do this, see Eskandarlou et al. (2023)). For each CCD, the flux ratios between SDSS and LBT sources have been calculated separately. The resistant (3σ rejection) median of these ratios was

[1] `https://www.sdss3.org/dr8/algorithms/magnitudes.php`

calculated, and the LIGHTS image was multiplied by this median to obtain pixel values expressed in nanomaggies.

3.1.3 Photometric calibration

It is important to perform astrometric and photometric calibration before stacking when working with images that may exhibit fluctuations in signal, noise, or instrumental effects Zaritsky et al. (2024). Science images are photometrically calibrated using SDSS DR12 images Alam et al. (2015). Due to the size of our FOV ($> 300 \times 300$), the SDSS tool 'mosaics' [2] was used. A pair of SDSS g and r-band images were created with a zeropoint of 22.5 mag. To calibrate the LBT image photometrically, around 600 (unsaturated) stars that range between 18 and 22 mag for both filters were used in both SDSS and LBT. There was no need to add a colour term between SDSS filters and Sloan LBT filters.

Using the Petrosian magnitudes obtained by SExtractor, the flux of the stars in the SDSS and LBT images has been determined. Since the SDSS images are photometrically calibrated, the photometric catalogue of the stars in SDSS was compared to the LBT catalogue, resulting in the following zero-points for the LBT images: $ZP_g = 34.527 \pm 0.006 \pm 0.01\,\mathrm{mag}$ and $ZP_r = 34.111 \pm 0.006 \pm 0.01\,\mathrm{mag}$ (the first error bar corresponds to the statistical error and the second error bar is the typical photometrical zeropoint calibration error reported by the SDSS team for these filters;Ivezić et al. (2004)). Based on the comparison of images of different quality and aperture sizes, it can be concluded that zero-point uncertainties are in the range of 0.01–0.02 magnifications Zaritsky et al. (2024). Therefore, it is the SDSS photometric accuracy that provides the ultimate precision for the LIGHTS survey.

3.1.4 Image Stacking

Since observational conditions change throughout the night, individual exposures are combined to create a final mosaic image Zaritsky et al. (2024). It is well understood that some of these variations can be controlled to some extent, such as those that are influenced by air mass and location of the target. Nevertheless, some events are unknown and out of our control, such as passing clouds that affect the brightness of the sky. The latter will generate artificially high standard deviations in sky pixel values, indicating a poorer image. In order to minimize these variations, images obtained under better conditions should be given greater weight in the final mosaic. The images were combined using a weighted average, with a weight for the ith image equal to the ratio of the standard deviation of the sky in the best exposure to the standard deviation of the sky in the ith image.

To compute the standard deviation of the sky in each image, bright sources and diffuse light were created using the procedure described in section 3.1.1. Then the 3σ clipping standard deviation of the non-masked pixels in each image calculated. Calculating the weighted mean is complicated by the fact that outliers, such as cosmic rays, strongly influence it. Typically, they appear as isolated pixels with high values that exceed the 3σ from the mean and NoiseChisel does not recognize them as sources. This type of pixel is defined as having a value that differs from the sigma-clipped mean of pixels at the same sky location, throughout all images. Therefore these outliers have been masked and using the sigclip—weighted mean routine in Gnuastro's Arithmetic program stacked

[2] `https://dr12.sdss.org/comingsoon/imaging/mosaics`

the data. As the co-added image is much deeper than any individual image, low surface brightness features become apparent, which were previously invisible. In fact, there are many features with very low surface brightness in the co-added image, probably because of the deep depth of the co-added image relative to an individual image Trujillo et al. (2021). It is these features, which include the extended wings on the stars, the stellar haloes surrounding galaxies, and the Galactic cirri, which affect the determination of the sky in our individual science images. Consequently, the sky determination process must be repeated for each exposure masking these regions. The final data co-add was then calculated using the improved masks generated by the first data co-add (and subsequent reduction steps described previously). For the specific case of NGC 3486, G.Golini et al. (2024, in preparation) provide a detailed quantification of each step of the data reduction pipeline.

The observational parameters, final image quality, and limiting magnitudes presented in Table 2 of the article by Zaritsky et al. Zaritsky et al. (2024). In Table 3.1, we present some of the LIGHTS target galaxies observational details only for the fields in which we conducted our research.

Name	$FWHM_g$ (arcsec)	$FWHM_r$ (arcsec)	air mass	FOV (arcmin)	$\mu_{\mathrm{lim},g}$ (mag,arcsec^{-2})	$m_{\mathrm{lim},g}$ (mag)	$\mu_{\mathrm{lim},r}$ (mag,arcsec^{-2})	$m_{\mathrm{lim},r}$ (mag)
NGC2712	1.03	1.00	1.24	37.7	31.83	28.22	30.85	27.06
NGC3486	1.60	1.59	1.07	40.2	31.36	27.10	30.54	26.38

Table 3.1: LIGHTS Target Galaxies: Observational Details

The quoted limiting magnitude and surface brightness limits refer to the regions within each field that have been observed for more than 70% of the total exposure time. A mask created from the deeper $g + r$ data was applied when calculating the surface brightness limits. For each image, the variance of the unmasked pixel values evaluated, adopting that value as an indicator of uncertainty within each pixel. Then the 5σ limit for a circular aperture with a radius equal to that of FWHM of each particular image calculated, to estimate the limiting magnitude and the 3σ limit for an area equivalent to a $10'' \times 10''$ box, to estimate the limiting surface brightness. Therefore, each pixel is assumed to be independent. It was found that the limits differed by approximately one magnitude across fields with the same exposure time. Some of this variation can be explained by differences in seeing conditions, air mass, scattered light, and light pollution, as well as proximity to the moon and its illumination. In the magnitude limit, the moon has the most obvious effect, although a large part of the variation is unaccounted for, presumably due to changes in atmospheric properties.

3.2 Hα data calibration and continuum removal

When analysing the star forming regions using narrow-band Hα filter data, removal of continuum is an important step. This continuum originates from observed celestial objects. In fact, although the used Hα filter has the spectral range from 6490 to 6646 Angstrom the Hα line alone, peaks at 656 nm. In order to isolate and analyze the emission characteristics associated with the Hα line only, it is critical to remove this continuum. In fact, the Hα emission happens to be in the observed range of the optical Sloan-r filter of LBT witch spans from 550.5 nm to 721 nm. To eliminate the continuum contribution from INT Hα data of our fields, Sloan-r data from LBT filter was used (G. Golini et al. 2024, in preparation). A critical component of removing continuum from the Hα

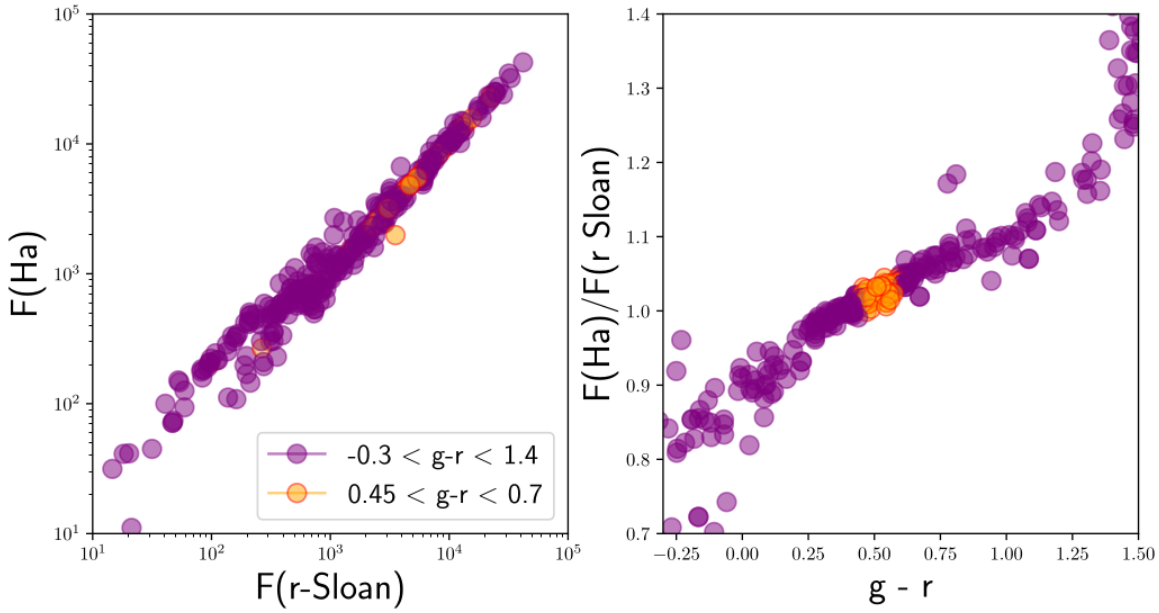

Figure 3.2: Relationships between fluxes of SDSS star spectra

image is applying a scaling factor.
The methodology for the calibration and continuum removal of these data processed by (G. Golini et al. 2024, in preparation) involves the following steps.
Initially, Skyviewer [3] is used to identify the precise SDSS photometry plate on top of the fields. Subsequently, R.A. and DEC. coordinates of all stars within the field with $0 < z < 0.1$ in the immediate 0.3-degree vicinity of the galaxy have been listed and saved. Specifically, non-saturated stars (with a magnitude range of $19 < G_{mag} < 22$) with known parallax have been retrieved. For each star corresponding SDSS spectra was downloaded and examined in order to measure the amount of Hα Flux (between 6490 to 6646 Å) the flux in the Sloan-r LBT filter (5505-7210 Å), and the flux in the Sloan-g LBT filter (3885-5845 Å) A linear relationship was found when the ratio of Hα light to r Sloan filter light was compared to the star's g-r color (Fig. 3.3): $\frac{F_{\mathrm{H}\alpha}}{F_r} = 1.02$ (g-r) + 1.4.

There is, however SDSS Fiber Aperture [4], to select a representative colour. Fig. 3.3 shows a large scatter around the linear relationship for certain colors (> 1 or < 0.2). So, the g-r color of the stars in the NGC 3486 field for example was determined using aperture photometry on LBT images with a d = 3 $''$ aperture.

There are two distinct peaks (one at g-r = 1.3, typical of red dwarf stars, and another at g-r = 0.5) in the distribution. In order to calibrate the flux, colors between 0.45 and 0.7 highlighted as orange dots in Fig. 3.3 we selected 30 stars. Bluer stars were chosen because of the greater scatter observed in the $\frac{F_{\mathrm{H}\alpha}}{F_r}$ versus g-r relationship with redder colors. In this case, $\frac{F_{\mathrm{H}\alpha}}{F_r}$ was calculated by selecting stars within this specific color range, resulting in an $\frac{F_{\mathrm{H}\alpha}}{F_r}$ ratio of 1.04 ± 0.14.

Knowing the ratio of the calibration and using aperture photometry with the same aperture employed previously, it is possible to compute the fluxes in both Sloan-r (from LBT) and $H\alpha$ data (from INT) of the selected stars. First step is aligning the Sloan-r and Sloan-g data from LBT to

[3] source:https://dr16.sdss.org/optical/spectrum/search
[4] source:https://www.sdss4.org/dr12/spectro/

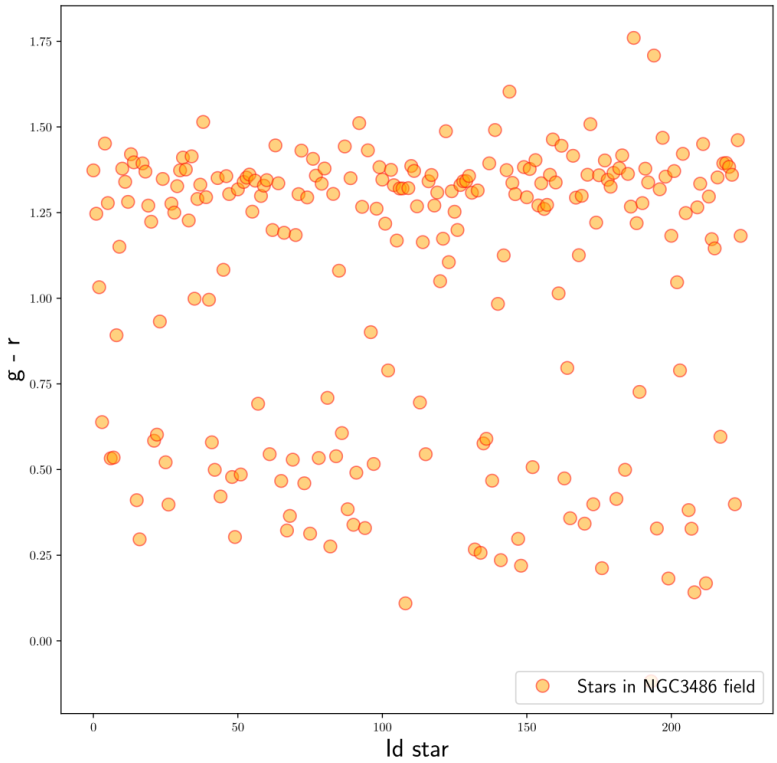

Figure 3.3: NGC 3486 field stars' g-r color distribution

the Hα image from INT. This process which results in a common pixel scale of 0.33″pix is crucial and was done using `"astwarp"` task from Gnuastro. After performing aperture photometry on both Hα and Sloan-r LBT datasets, the ratio between the two datasets was assessed and the Halpha Flux in the INT data (FHa,INT) was 1000 times greater than the Sloan-r LBT flux (Fr,LBT). As next step, the INT flux was adjusted and so that the ratio $\frac{F_{\mathrm{H}\alpha,\mathrm{INT}}}{F_{r,\mathrm{LBT}}} = 1.04$ equaled 1.04. In order to determine only the contribution of the Hα image, the aligned Sloan-r (LBT) subtracted directly from the Hα image which resulted in so-called Hα emission.

3.3 Catalog-making

After calibration and corrections done on the images (G. Golini et al. 2024, in preparation), catalogs of them have been built (Z.Hosseini-Shahisavandi et al. 2025, in preparation).
The Gnuastro programs were used for detecting and segmenting the images in order to make the catalogs for r and g Sloan filters.
First step is detection which is the process of separating the pixels in the image into two groups of 1) Signal, and 2) Noise. In order to separate the signal (galaxies or stars,...) from the background noise in the images Gnuastro's NoiseChisel was used. NoiseChisel's output contains 5 extensions. The first (or zero-th) extension of the output contains meta-data which are information about/describing the datasets within (all) the output's extensions. The second extension (INPUT-NO-SKY) represents the input with the sky subtracted. Third one (DETECTIONS) is NoiseChisel's main output which is a binary image with only two possible values for all pixels: noise 0 and signal 1. Fourth and fifth extensions (SKY and SKY-STD) have the Sky and its

standard deviation based on undetected regions on a tile grid.
As next step, in order to find the individual galaxies/peaks over the detected pixels, segmentation was done on the noisechisel results to build the segmentation map. The output of segment's operation is also a multi-extension FITS file. What Segment does as first step is to finds true clumps over the detections. Local peaks (maxima or minima) define the formation of clumps, which extend across nearby pixels until they reach a local valley (river/watershed). To find "true" clumps, Segment uses the distribution of clump signal-to-noise ratios over undetected regions as a reference. Once the detections have been made, these true clumps are then grown to a certain threshold. Growing clumps are either considered parts of one object or separate objects based on the strength of the connections between them (rivers/watersheds) (see Akhlaghi and Ichikawa (2015) for more). The main outputs of the segment are two labeled datasets: 1) CLUMPS, and 2) OBJECTS.
On the other hand, obviously a dataset (for example, an image) is simply a collection of values, placed after each other in any number of dimensions. Basically, every element of data (pixel) has two properties: position (relative to other elements) and value. To do the analysis we have to know/measure the properties of the (separate) scientifically interesting targets that are embedded in it such as, the magnitudes, positions and elliptical properties of the galaxies that are in the image. Gnuastro's MakeCatalog program allows localized measurements to be made on a dataset and convert low-level datasets (like images), to high level catalogs containing measurements on pixels with specific labels. As an output of MakeCatalog, a catalog with two extensions was built using segmentation maps. Measurements over OBJECTS are shown in the first extension, while measurements over CLUMPS are shown in the second extension. The CLUMPS catalog has been used to study the CLUMPY structures and fragmentations on top of the Galaxy, while the object catalog give us the information about the galaxy as one source.
For our research we use three filters of Sloan-g, Sloan-r and Hα filters. To field the reference filter, the depth of images was checked and the surface brightness limit (3σ, over 100 $arcsec^2$) and 5 sigma limiting magnitude with apertures with radius of 2 FWHM (upper limit magnitude) for each filter calculated. An upper limit magnitude is found by placing the circular aperture with **radius?** of 2 FWHM over an area without detections and measuring the sum of pixel values within the footprint. The standard deviation (σ) of this distribution can be used to quantify the upper limit magnitude (given its particular shape and size). Based on these measurements, the g filter is found to be the deepest of the three. Meaning that the sources seem to be more sharper and more detectable through this filter. Since we are interesting to investigate all the possible star forming clump, we use the segmentation map of the deepest filter as the reference filter for doing photometry and making catalogs. When we select a reference filter, we can study the same structures in all three filters (g, r, and Hα); these structures are referred to as CLUMPS. Therefore, taking the Sloan-g filter as reference filter, catalogs for each filter was built (Z.Hosseini-Shahisavandi et al. 2025, in preparation).
Our research was conducted with these catalogs that contain IDs, positions, sums, magnitudes, etc. The next characteristics that will be described later are added to these catalogs. Prior to any operation, it is important to make sure that the pixels of the filters are the same size. In our case, g and r images taken by LBT have the same pixel size of 0.224 arcsec and on the other hand, Hα images captured with INT have pixel size of 0.33 arcsec. It is therefore necessary to re-grid the Hα image to ensure that we are calculating the magnitude of Hα on the same area of the sky on top of the Galaxy.
Detailed descriptions of the properties are available in GNU Astronomy Utilities and we will touch on a few of them here:

Very first thing they have is ID which is the identifier. There are various identifiers in general but in our case, we have "obj-id" in OBJECT catalog and "host-obj-id" and "id-in-host-obj" in CLUMPS catalog which are ID of object, ID of the object which hosts this clump and the ID of this clump in its host object respectively.
On the other hand, there are Right Ascension ("RA") and Declination ("DEC") columns present in the catalogs which are the most common WCS coordinates in an equatorial system. To get their values, the algorithm gets flux weighted right ascension and declination of all objects or clumps. Using the FITS WCS keywords (CTYPE), MakeCatalog determine which axis corresponds to the RA/DEC.
The other set of columns in the catalogs are the measurements that only deal with the pixel values ignoring the pixel positions.
For example "sum" is simply the sum of all pixel value (object or clump) and "magnitude" is the magnitude of the clumps or objects. Note that the sky value of image will be subtracted before any column measurement. For clumps, the ambient values (average of river pixels which are surrounding and outside the clump Akhlaghi and Ichikawa (2015), multiplied by the area of the clump) is subtracted. But the next column called "sum-no-river" is just the sum of Sky (not river) subtracted clump pixel values.

3.4 Star forming clumps selection

We are primarily interested in studying clump properties as we move away from the center of the galaxy and we concentrate on clumps where probably star formation is taking place. Therefore, in this analysis, accurate selection of star-forming clumps and their property derivation play an important role. Employing the new data analysis techniques available today with Gnuastro, we tried to select the suspected star-forming regions of the main central galaxy in each field and to do this more proprieties are needed to be added to the initial catalog introduces in section3.3. In this section, we will first introduce colors and the elliptical distance (real distance) of the clumps from the center of the galaxy that will be added to the catalog (section3.4.1) and then we will examine the selection of stars forming clumps candidates and estimate the contamination level (section3.4.2).

3.4.1 Color and distance of the clumps

All the steps and analysis will be introduces in this section applied on both NGC2712 and NGC3486 galaxies' images.
We will introduce two important properties that we will be used frequently in our analysis. To do this, after selecting only the central galaxy clumps, two colors were calculated through three chosen filters. In fact, using Sloan-g filter as reference image, we derived two colors of g-r and g-Hα by subtracting magnitude values of each clump in r and Hα filters from g filter clumps.
Another important property is the clumps' distance from the galaxy's center. The elliptical distance is what we are looking for and refers to how far a point is from the center of the galaxy considering the orientation of the galaxy with respect to our line of sight. Understanding distance is key to getting this.

Fig. 3.4 shows a simple example of a case in which the solid red line shows the real shape of a galaxy, while what we see is the dashed line in elliptical shape due to our line of sight. Therefore, we

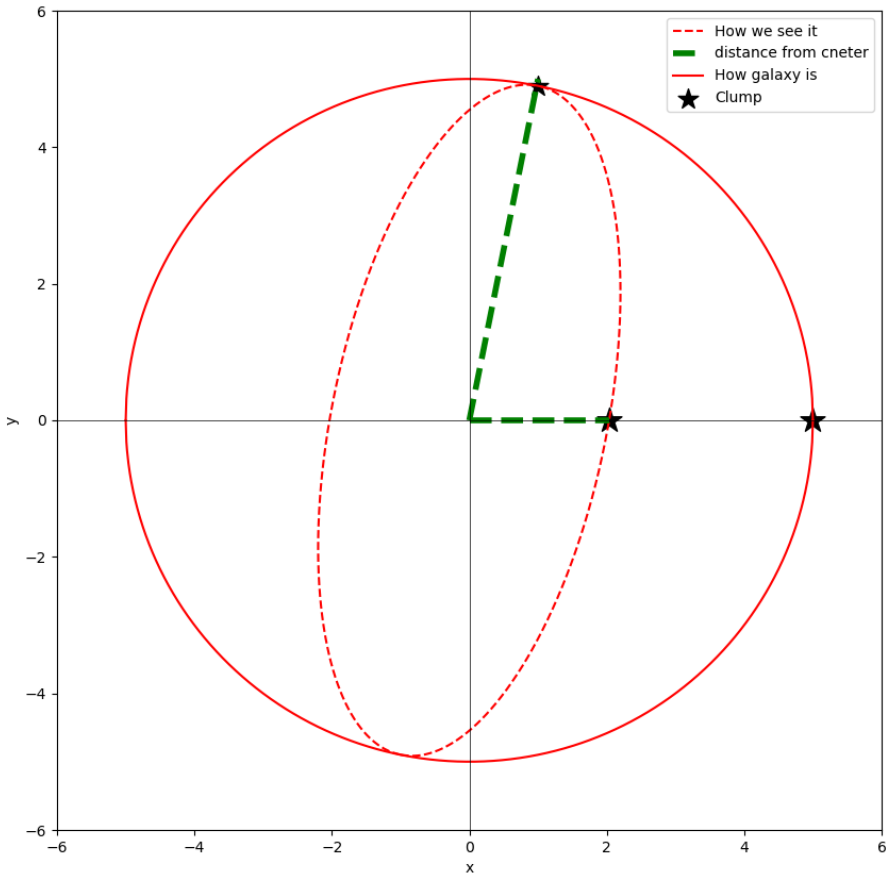

Figure 3.4: The schematic shows an elliptical distance concept simplified. The solid red line represents the true shape of the galaxy, while the dashed red line represents its apparent shape as observed. Green dashed lines representing the measured distance between the galaxy's center and each clump are expected to have the same size.

can agree that distance of clumps located on any part of the ellipse (in this image semi-major axis and semi-minor axis) are at the same distance (green dashed lines) from the center of the galaxy even though it might seem different due to projected shape on the plane of the sky. To calculate this distance, we must first agree that no matter how much or in which direction the galaxy plane rotates, we will have just one angle between the galaxy plane and celestial sphere plane which is called inclination. The inclination of both galaxies was determined using equation (3.1, where i is the inclination, a and b are the semi-major and semi-minor axes respectively. Table 3.2 shows these values for our case.

$$i = \cos^{-1}\left(\frac{b}{a}\right) \tag{3.1}$$

The goal is to place a radial profile of any functional form f(r) over an ellipse. Therefore, every point in space must be given a radius or distance. In this regard, radial distance r_{el} can be defined

Galaxy	axis-ratio(q)	inclination(i)(degrees)
NGC 3486	0.76	56.63
NGC 2712	0.55	40.54

Table 3.2: Axis ratio and inclination of NGC 3486 and NGC 2712

as the distance on the major axis to the center of an ellipse located at i_c and j_c (in other words, $r_{el} \equiv a$). Specifically, the objective is to find r_{el} of a point(clump) located at (i, j), in the image coordinate system, from the center of the ellipse. To do this, we will draw an ellipse passing through this CLUMP such that its q is the same as the galaxy (though it may have different a and b) and its center (where the semi-major and semi-minor axes coincide) is on top of the original galaxy's center (Fig. 3.5). Using the ellipse definition and the assumption that $r_{el} \equiv a$, we get

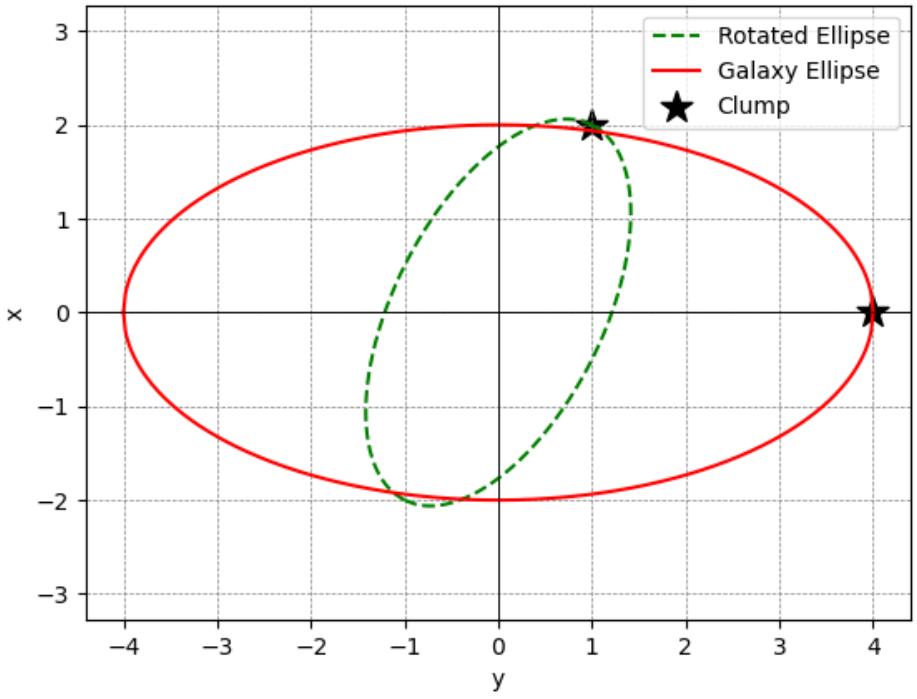

Figure 3.5: Illustration of elliptical distance calculations for clumps at random positions. Red ellipse represents galaxy centered at origin. The green dashed shows ellipse with the same axis ratio and center locating clump at its semi-major axis.

the elliptical distance as equation (3.2). Therefore, generalizing this approach, we can notice that the axis ratio of the galaxy and the coordinates of the clumps are the only parameters needed to determine the distance of each clump. As before, an ellipsoid or an ellipse in 3D can be defined with similar principles.

$$r_{el} = \sqrt{i^2 + \left(\frac{j}{q}\right)^2} \tag{3.2}$$

In Gnuastro, "astscript-radial-profile" is responsible for calculating radial profile of objects in the images that results in the light distribution of galaxy as function of radial distance from center (Fig. 3.6). In fact, "astscript-radial-profile", apart from resulting in radial profile, will also result in an image that shows the distance in 2D called "aperture" in which, each color has a value and shows the same distance distance from center of the galaxy (up left image in Fig. 3.6). In order to get the value of distance for each clump, a point like source at the right ascension and declination of each clump was used that as a result of overlapping it on the aperture, each clump in the galaxy was assigned a distance value.

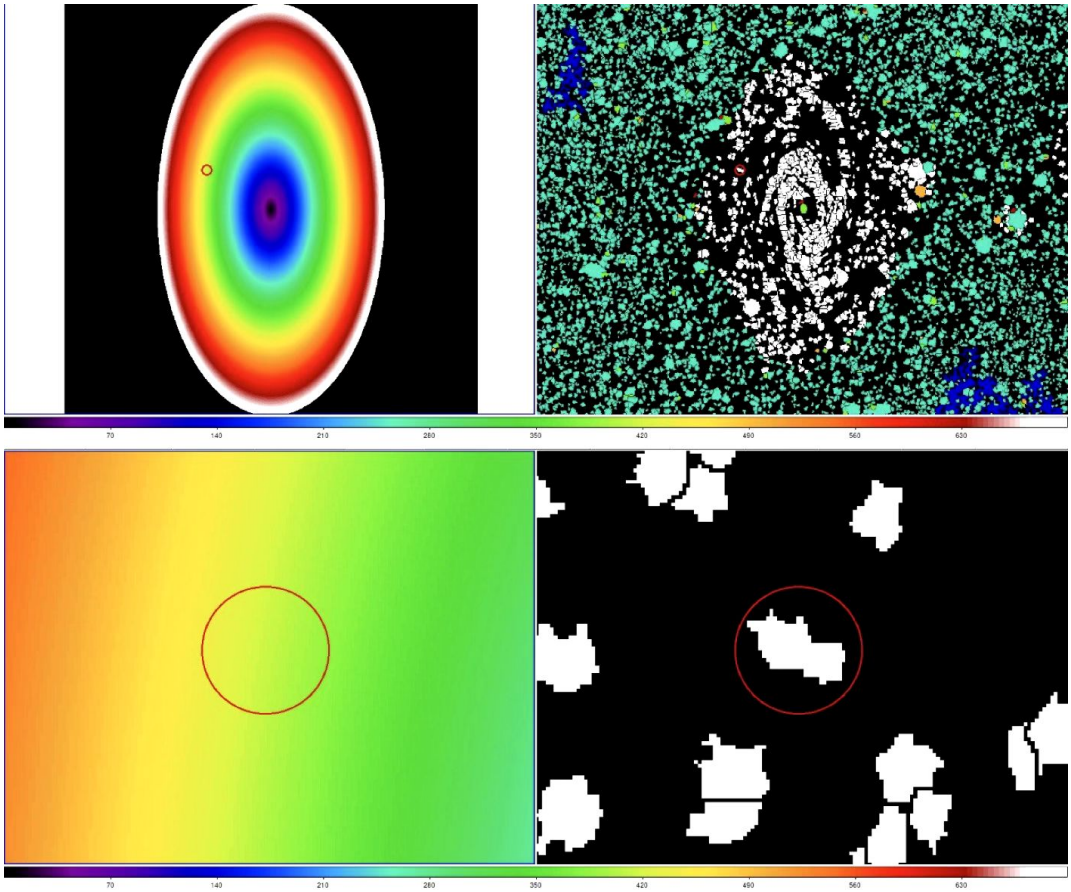

Figure 3.6: Radial profile of NGC 2712 and clumps extension of the same galaxy. Colors in the radial profile show the distances.

3.4.2 Star forming clumps candidates selection

One of the main steps of this work is the accurate selection of star-forming clumps. H-alpha emission will be used in this process as it is expected to be dominant in regions where star formation is in progress. In order to do this, color magnitude diagrams (CMD) were used, taking into account that the reference filter is the g band. Fig. 3.7 and Fig. 3.8 show the clumps distribution of NGC 2712 and NGC 3486 galaxies respectively in CMD in which color shows the distance of each clump from the center of the galaxy that was derived in (section3.4.1).
CMD with g-Hα color was chosen in order to estimate limits for real galaxy clumps because it shows a greater separation for elliptical distance compared to CMD with g-r color. As part of the

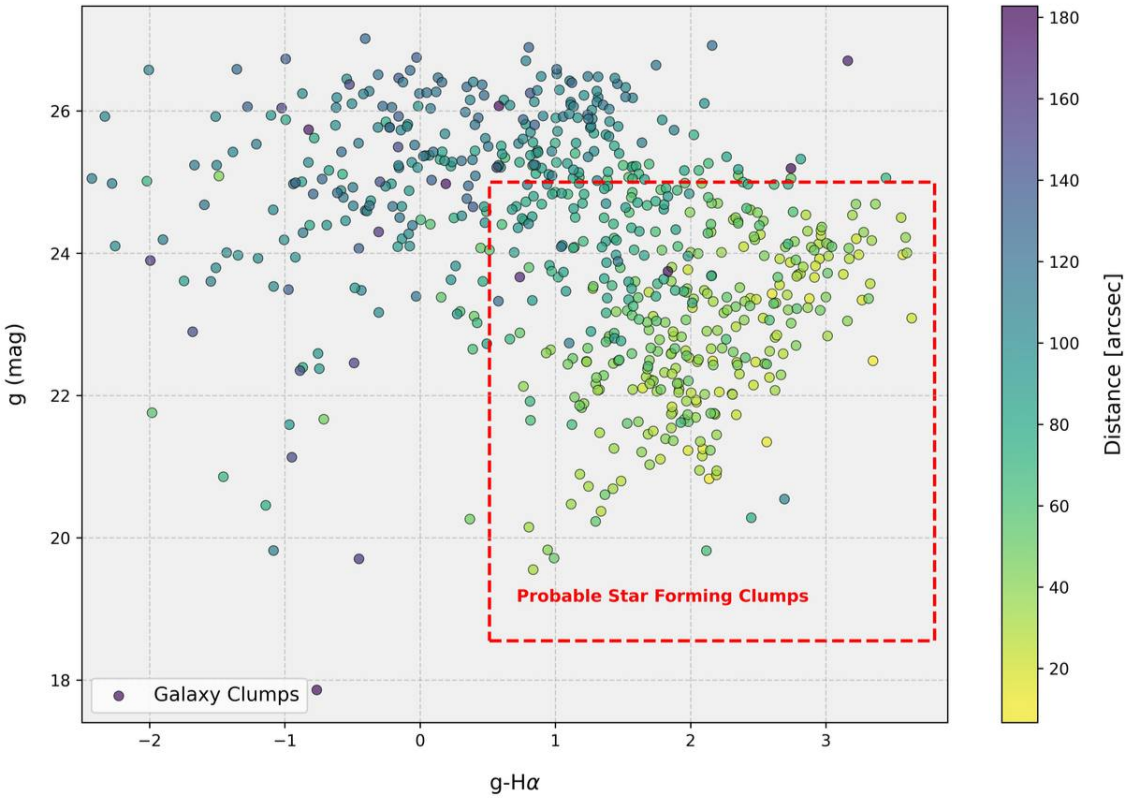

Figure 3.7: color magnitude diagram of NGC 2712 color coded by the distance of the clumps from the center of the galaxy. Red square shows the selected probable star forming clumps.

selection process, both color and magnitude were considered in such a way that for both galaxies, colors of above 0.5 were chosen to include clumps emitting Hα light, whereas another selection was done by looking at magnitudes in such a way that magnitudes below 25 for NGC 2712 and below 24.5 for NGC 3486 were considered as trustworthy ones that aren't influenced by noise. As a result, the selected star-forming clumps candidates of each galaxy have been shown in Fig. 3.7 and Fig. 3.8, which are enclosed in red dashed line.

It is important to realize that these are not accurate selections since there may be contamination from sources present in the galaxy's foreground and background. As such, estimating contamination is the next crucial step for which we need to find the usual color and magnitude of the field where the galaxy is present. Hence, we start by masking all detectable sources in the field, leaving only the sky (Fig. 3.9 and Fig. 3.10). By taking the same steps as we did for the central galaxies, we can create a catalog of the masked region, including the same colors and magnitudes. Creating color magnitude diagrams as Fig. 3.7 and Fig. 3.8 but this time for the masked region, we can apply the same selection for each galaxy's masked field.

To further analyze the results, we used this masked field to create a 2D histogram and get an idea of the clumps number density with specific colors and magnitudes. In order to account for the difference in coverage, each value in the histogram was divided by the ratio of the galaxy area to the masked area. In this way, we were able to obtain the contamination density per bin, which represents the expected level of contamination in that area of the color-magnitude space. Hence, all we need to do to find the contamination is to plot the selected clumps in Fig. 3.7 and Fig. 3.8 on a two-dimensional histogram of each field (Fig. 3.11 and Fig. 3.12 respectively), which allow us to

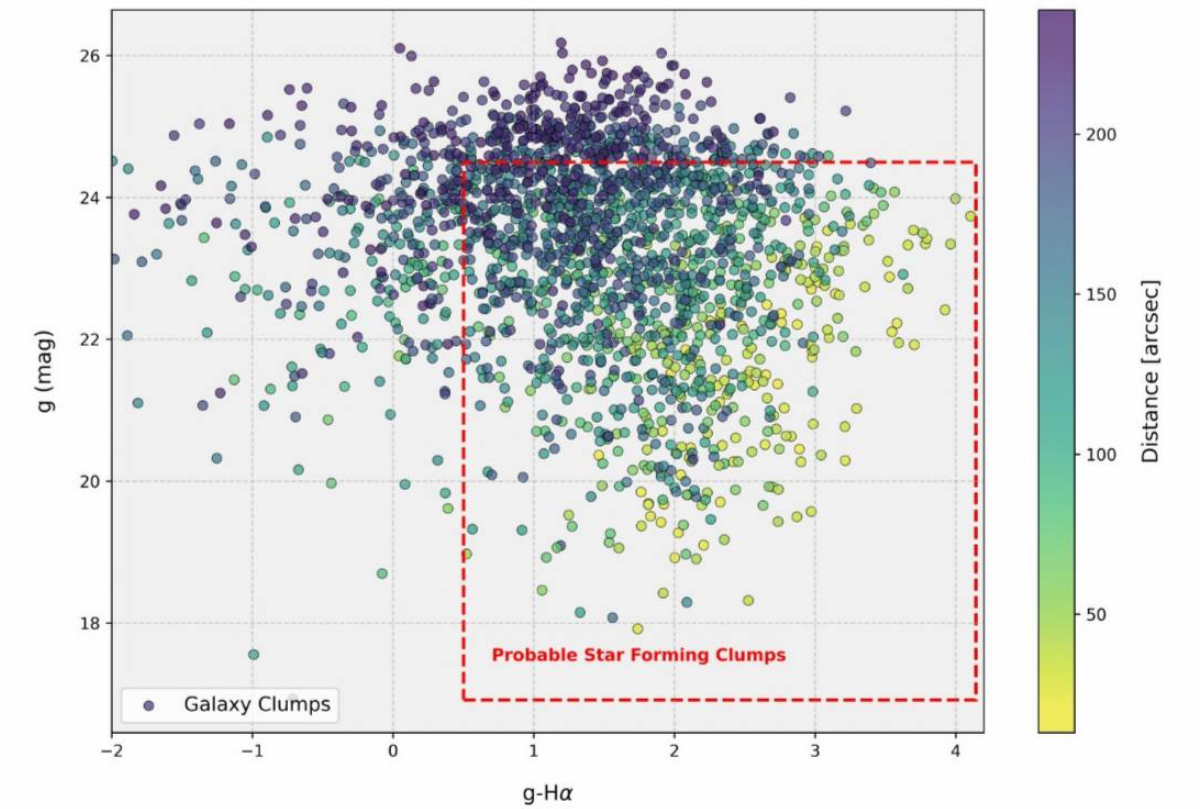

Figure 3.8: Color magnitude diagram of NGC 3486 color coded by the distance of the clumps from the center of the galaxy. Red square shows the selected probable star forming clumps.

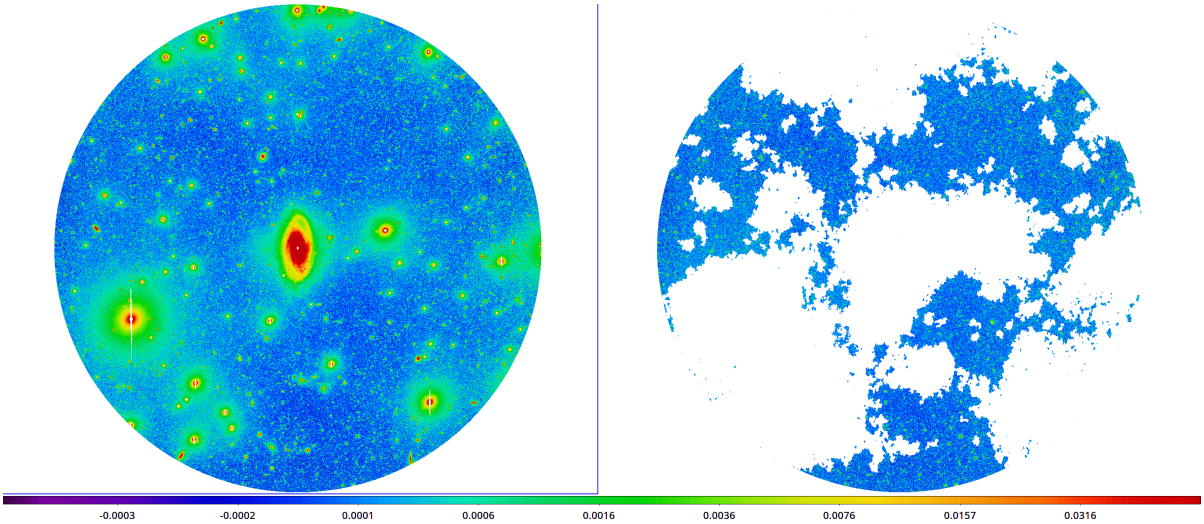

Figure 3.9: The left image illustrates the input-no-sky extension of NGC 2712, and the right image depicts the same imaged with masked objects

assign each clump a number as contamination, or, in other words, assign each clump a weight. A specific contamination value was assigned to each star-forming clump by dividing its corresponding bin value by the number of clumps present in the bin. As a result, the position of individual clumps in the 2D color-magnitude space allowed for a more accurate estimation of contamination.

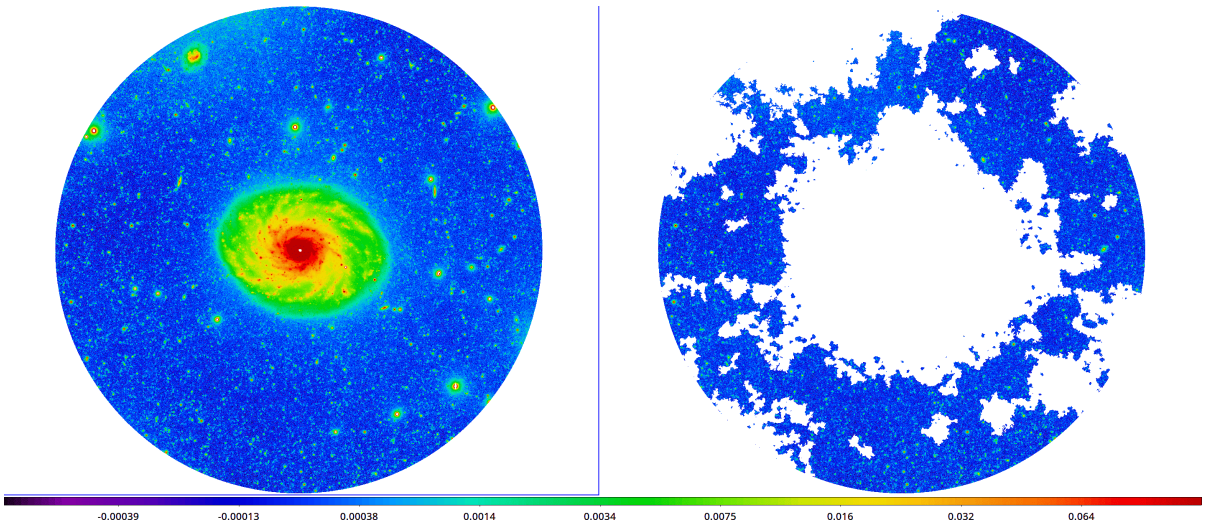

Figure 3.10: The left image illustrates the input-no-sky extension of NGC 3486, and the right image depicts the same imaged with masked objects

The color code in the histograms of Fig. 3.11 and Fig. 3.12 referred to as contamination, ranges

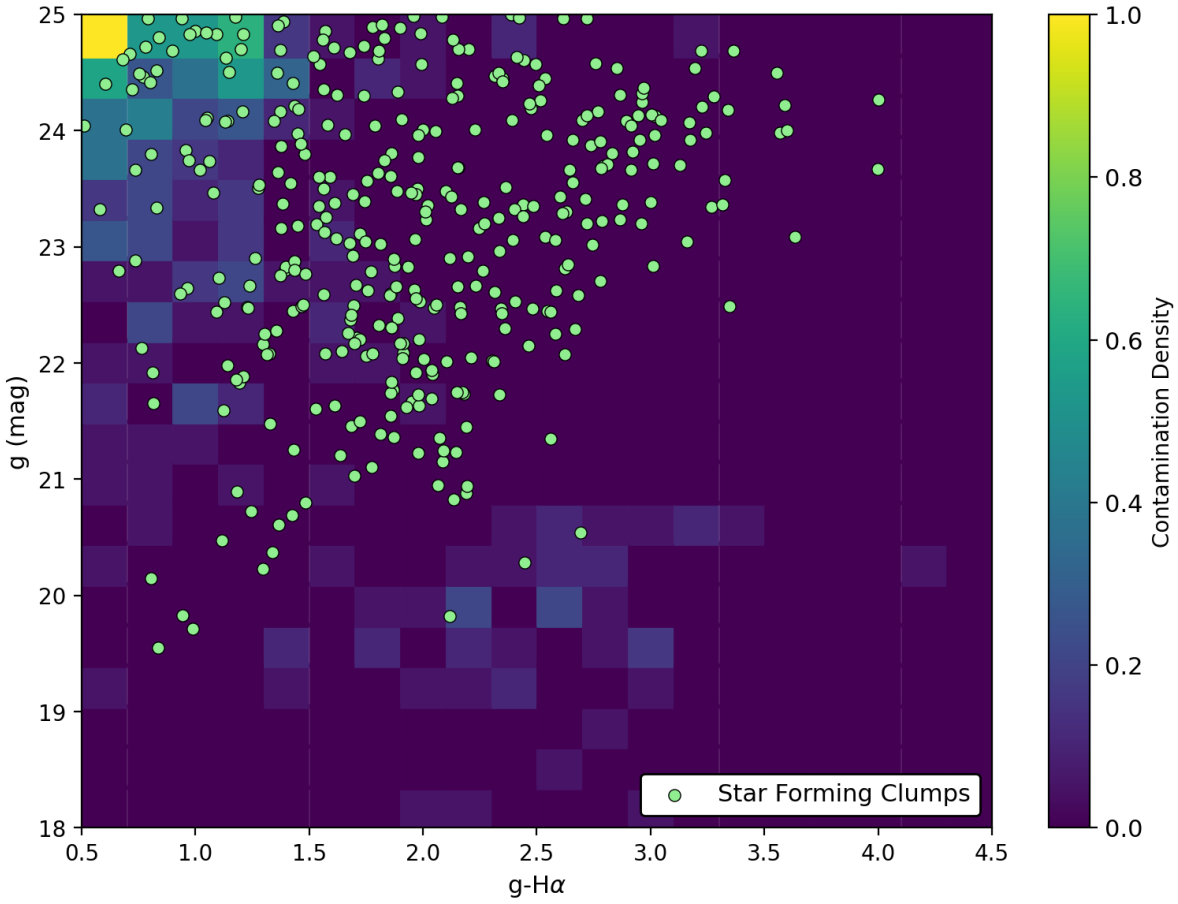

Figure 3.11: Star forming clump candidates of the NGC 2712 galaxy overlaid onto the masked region CMD 2D histogram. Color-bar shows the contamination.

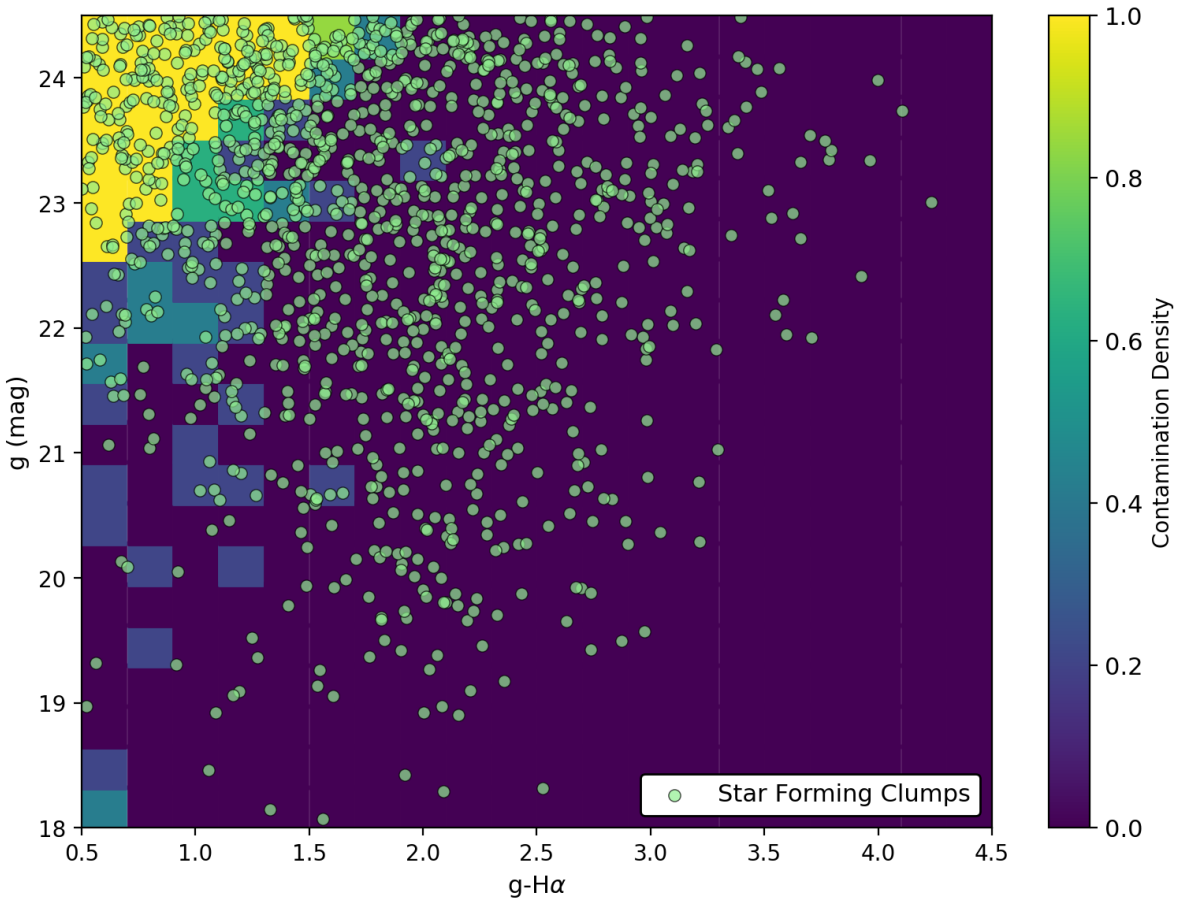

Figure 3.12: Star forming clump candidates of the NGC 3486 galaxy overlaid onto the masked region CMD 2D histogram. Color-bar shows the contamination.

from 0 to 1 in which 0 indicates that the clump is not contaminated or, in other words, that it belongs to the galaxy. Whenever the value of contamination increases and approaches 1, the amount of contamination increases, which states that the clump with a contamination value of 1 is not from the galaxy. Following the identification of the candidates of star forming regions and their contamination probability, we can proceed to the analysis which will be explained in detail in section4.

Chapter 4

Results and Discussion

In this section having star forming clump candidates, we can explore their properties as we go away from the center of the galaxy. Our aim is to investigate the star formation activities in the outer low surface brightness region by studying the color and magnitude of these two galaxies.
There are several notable trends and differences between star-forming clumps at the edges of NGC 3486 galaxy at distance of 13.6 Mpc and NGC 2712 galaxy at 30.2 Mpc , compared to those in the central regions, that shed light on the nature of star formation in these low-density environments. The first results are shown in Fig. 4.1 and Fig. 4.2 which are the g-band magnitude of selected star-forming clumps as a function of their distance from the galaxy center. The blue line in the figures shows the trend considering the contamination. This trend shows that magnitude decreases as distance increases, indicating fainter clumps at larger radii. It is evident from the color bar that contamination is not high, therefore the trend can be trusted since it is not biased by contamination.

This trend, visible in both galaxies, is consistent with the idea that the outer regions of the galaxies are characterized by lower stellar densities and this increase in magnitude with distance implies that the material available for star formation decreases towards the outskirts, leading to less luminous star-forming regions. In fact, as we move away from a galaxy's center, magnitude decreases because there are fewer stars and luminous material, leading to a gradual decline in brightness compared to the central, star-rich region. Consider that the inset plot represents an error analysis based on a mock profile simulation. For this purpose, a set of artificial clumps with known magnitudes was created utilizing real stars present in the image, and then inserted them into regions of the image which were free of sources, and by retrieving the magnitudes using noisechisel and segment from Gnuastro, we remeasured the original magnitudes. In this plot, magnitude of simulated mock profiles (original magnitude) was plotted against the standard deviation of difference between the original magnitudes and the measured magnitudes.
In particular for faint sources that are more likely to be corrupted by noise and systematic errors, this serves as an important diagnostic to determine the reliability of magnitude estimates.
On the other hand, the g-r color distribution as a function of distance provides further insight into the differences between star-forming clumps at various radii (Fig. 4.3 and Fig. 4.4). The plot suggests that the g-r color remains relatively constant across the disk in both galaxies. In contrast to the magnitude trend, g-r trends are relatively flat, suggesting that while stellar content in the outskirts is fainter, it retains the same overall color as those in the center. Same as Fig. 4.1 and Fig. 4.2, the blue line in these plots shows their trend considering the contamination.

The final plots of g-Hα versus distance from the galaxies center show the most pronounced

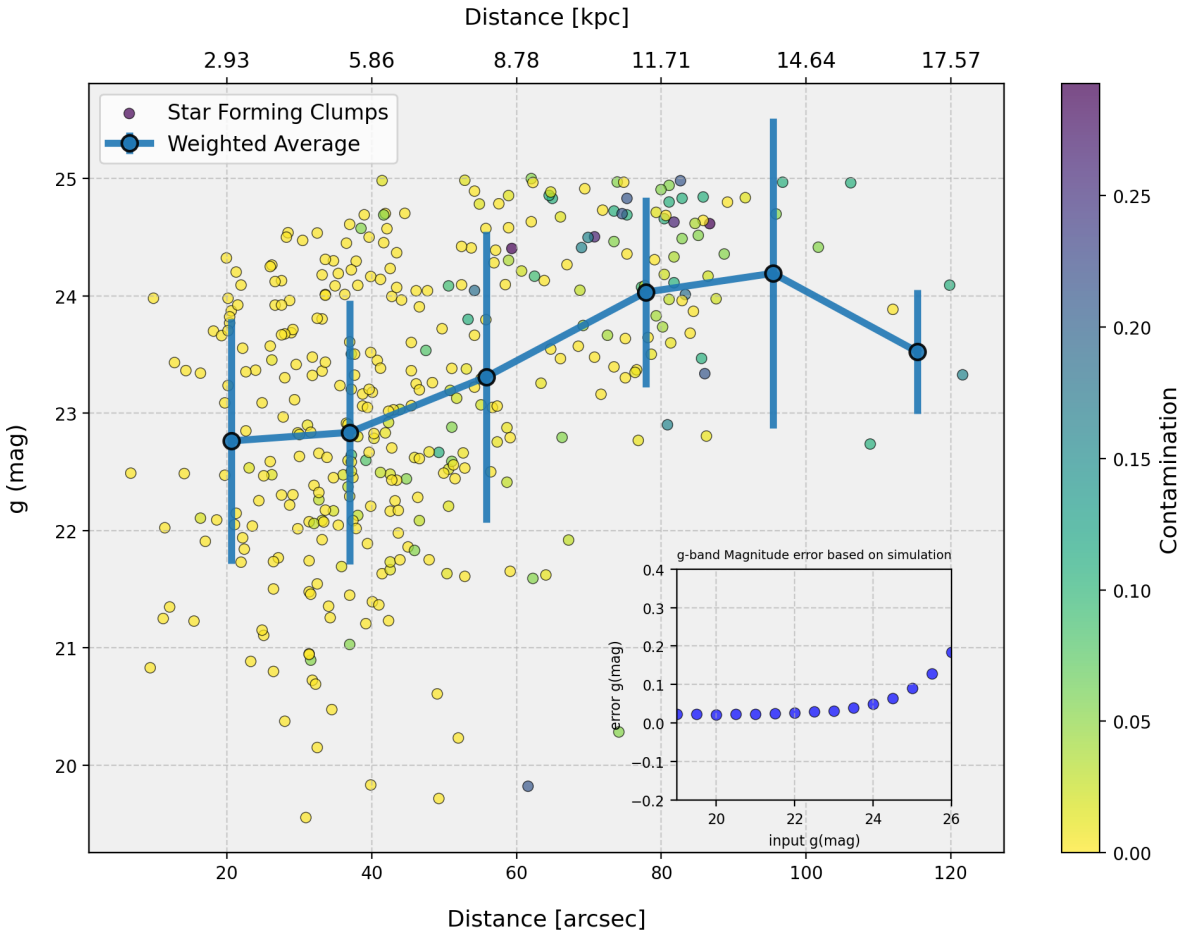

Figure 4.1: NGC 2712 g-band magnitude of star-forming clumps as a function of their distance from the galaxy center color coded by contamination. Error bars represent the standard deviation of the weighted average in each distance bin, shown symmetrically in both directions. The inset plot represents error analysis based on mock profile simulations

gradient, with a clear decrease in g-Hα as the distance increases (Fig. 4.5 and Fig. 4.6). Take into account that the error bars in these plots are representing the standard deviation of the weighted average values of data in each radial bin, shown in both the positive and negative directions. The g-Hα color traces the amount of Hα emission with respect to the g-band, providing a measure of the ongoing star formation rate. As g-Hα decreases towards a larger distance from the center, there is a significant reduction in Hα emission in the outer disk, suggesting that the star-forming clumps have lower levels of ionized gas in these regions, which directly reflects reduced star formation activity in these regions. The aforementioned trend indicates that while star formation is still present at the edges of both NGC 2712 and NGC 3486 galaxies, it is less efficient and less intense than in the central regions. It may be due to a reduction in gas availability in the outskirts, which causes fewer ionizing photons and less intense star formation.

On the other hand, the color bars indicate that contamination remains fairly uniform across distances, with a slight increase at larger radii. On the other word, this imply that the star-forming clumps in the outskirts are experiencing a quiescent mode of star formation. The results suggest clumps on the outskirts may be affected by background objects and observational artifacts with low probability, which in any case should be taken into account when interpreting them.

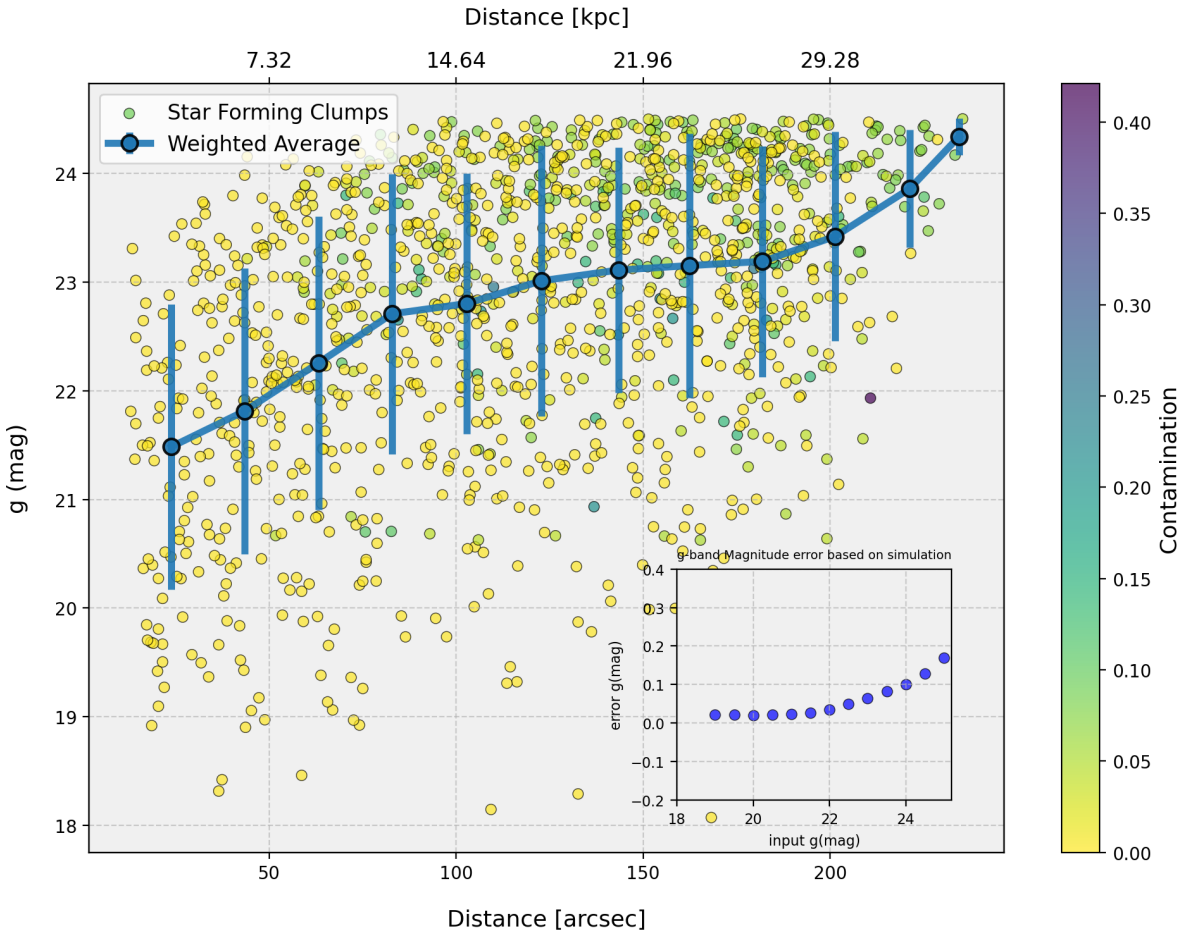

Figure 4.2: NGC 3486 g-band magnitude of star-forming clumps as a function of their distance from the galaxy center color coded by contamination. Error bars represent the standard deviation of the weighted average in each distance bin, shown symmetrically in both directions. The inset plot represents error analysis based on mock profile simulations.

The overall trends, however, point to a consistent decline in star formation activity and stellar luminosity with increasing distance from the galaxy center.
These findings have important implications for understanding the current rate at which galaxy disks are growing. The differences in star formation efficiency, traced through the g-Hα color, may highlight the role of environmental factors such as gas density, cooling rates, and tidal interactions in regulating star formation at the edges of galaxy disks.
Findings like these play a critical role in understanding the mechanisms that drive star formation in the lowest surface brightness regimes at the edge of galaxy disks. Various future studies, including kinematic analyses and comparisons with other galaxies, may provide more insight into whether these trends are unique to NGC 2712 and NGC 3486 or a common feature of spiral galaxies.

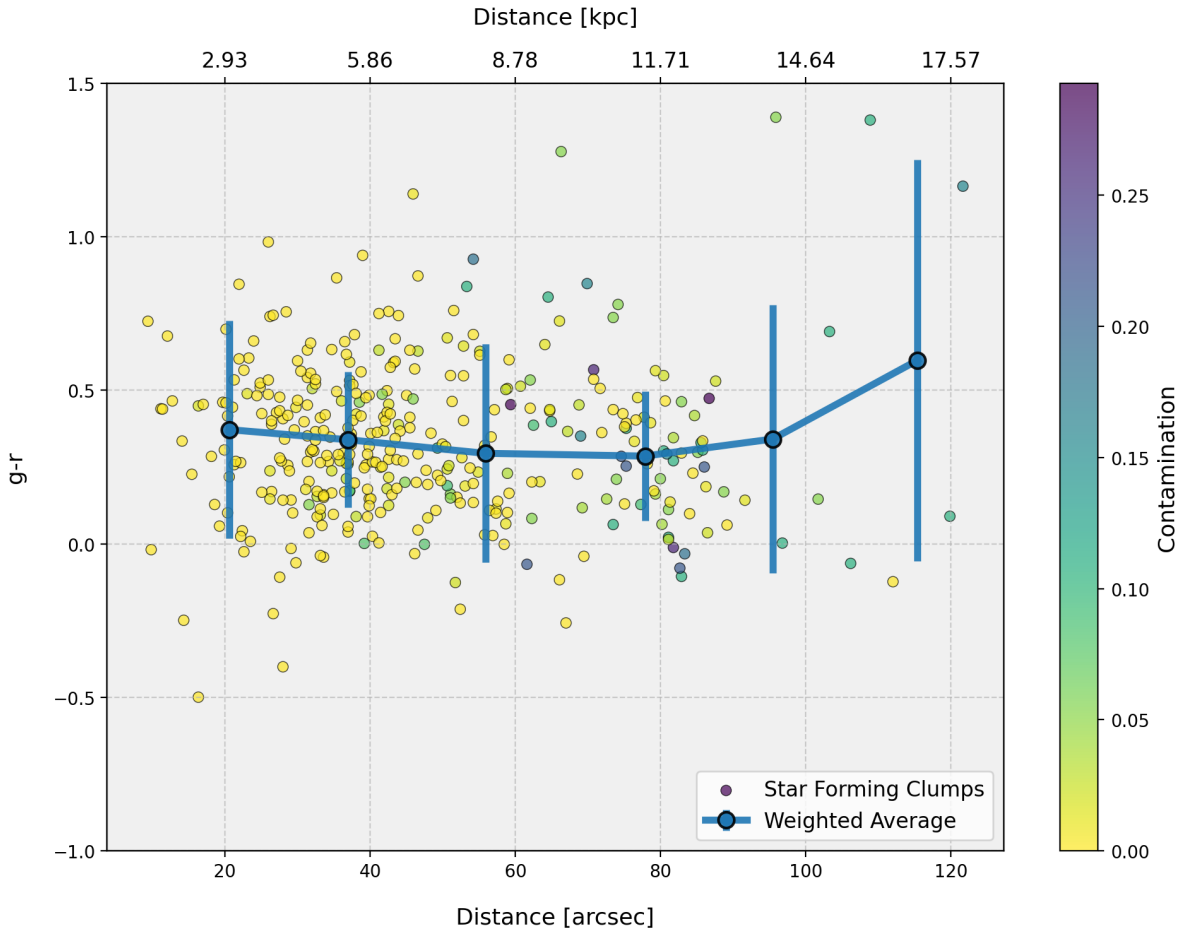

Figure 4.3: NGC 2712 g-r color of star-forming clumps as a function of their distance from the galaxy center color coded by contamination. Error bars represent the standard deviation of the weighted average in each distance bin, shown symmetrically in both directions.

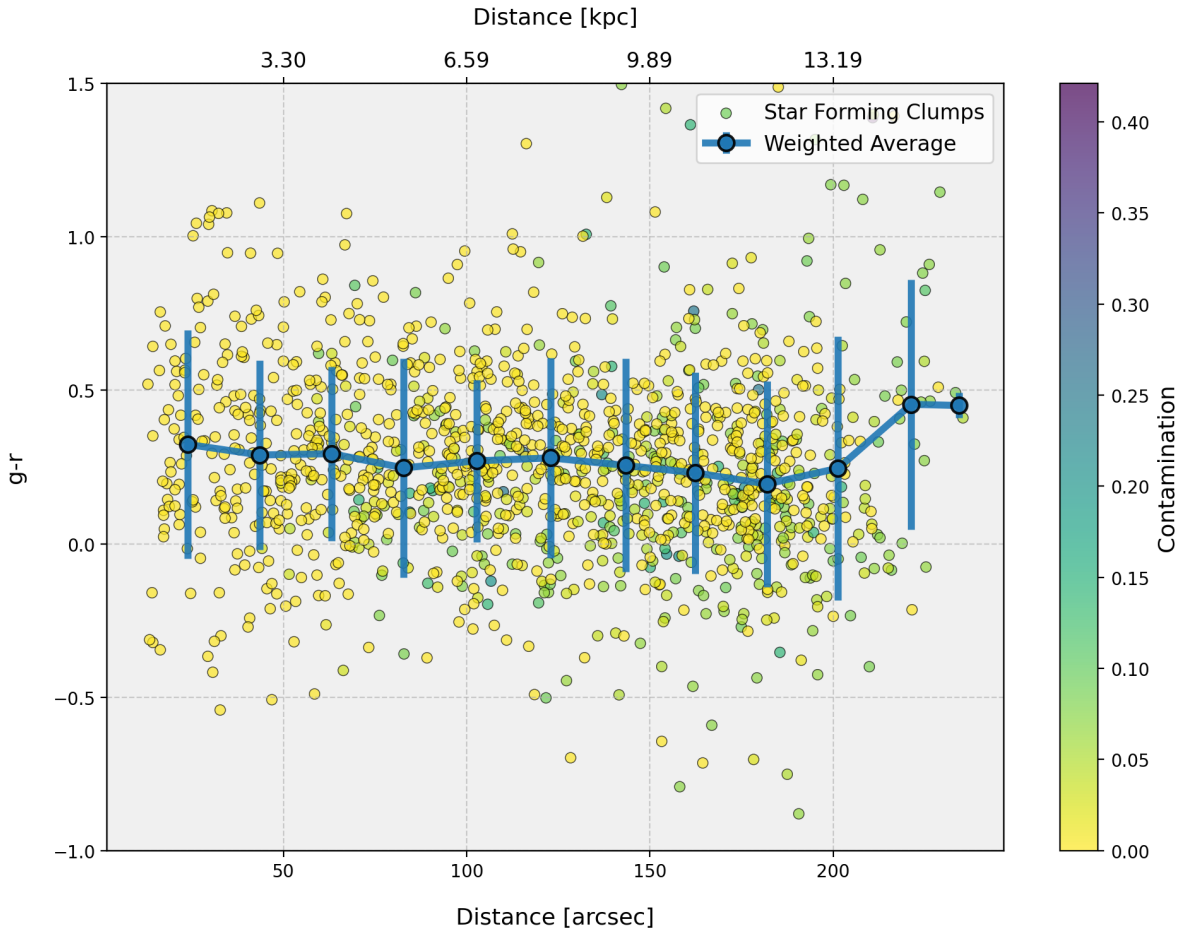

Figure 4.4: NGC 3486 g-r color of star-forming clumps as a function of their distance from the galaxy center color coded by contamination. Error bars represent the standard deviation of the weighted average in each distance bin, shown symmetrically in both directions.

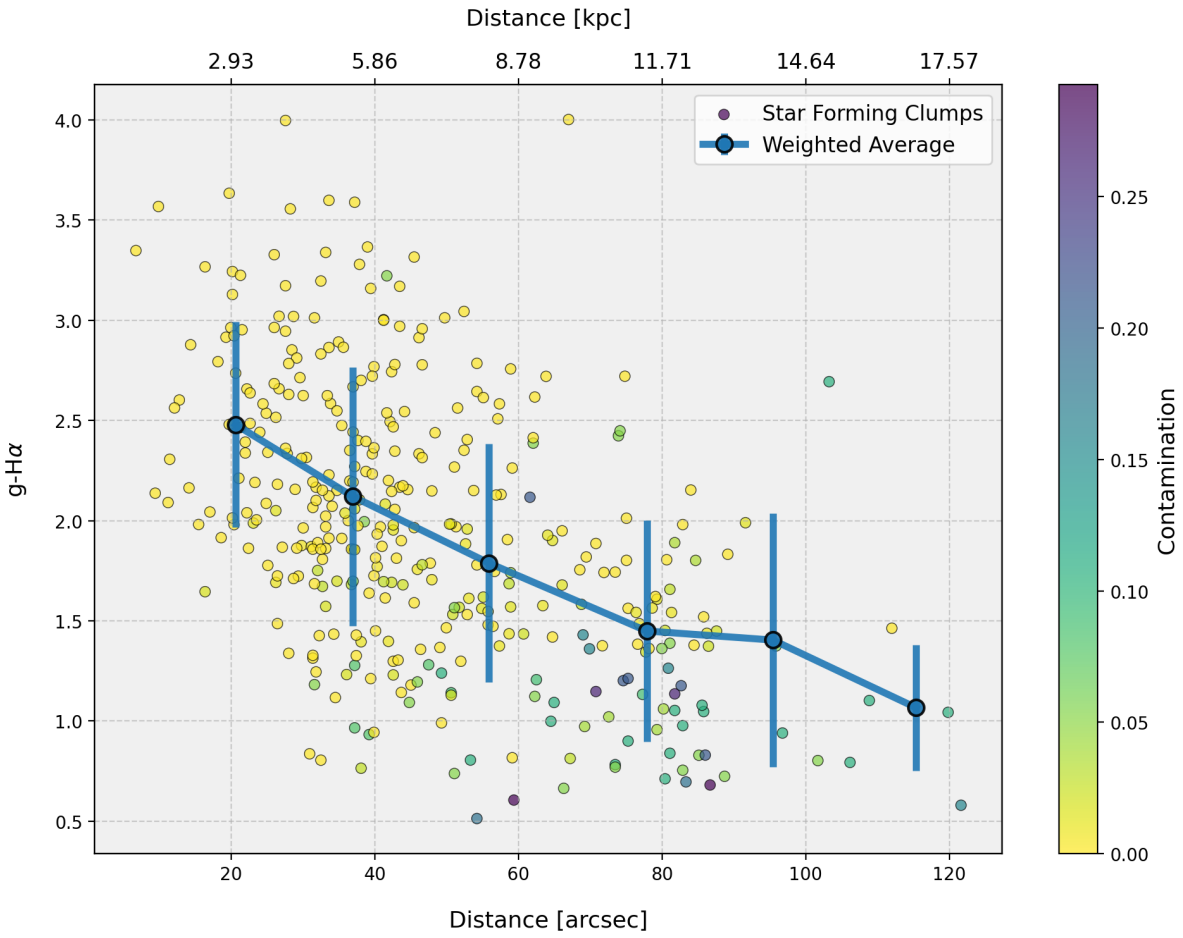

Figure 4.5: NGC 2712 g-Hα color of star-forming clumps as a function of their distance from the galaxy center color coded by contamination. Error bars represent the standard deviation of the weighted average in each distance bin, shown symmetrically in both directions.

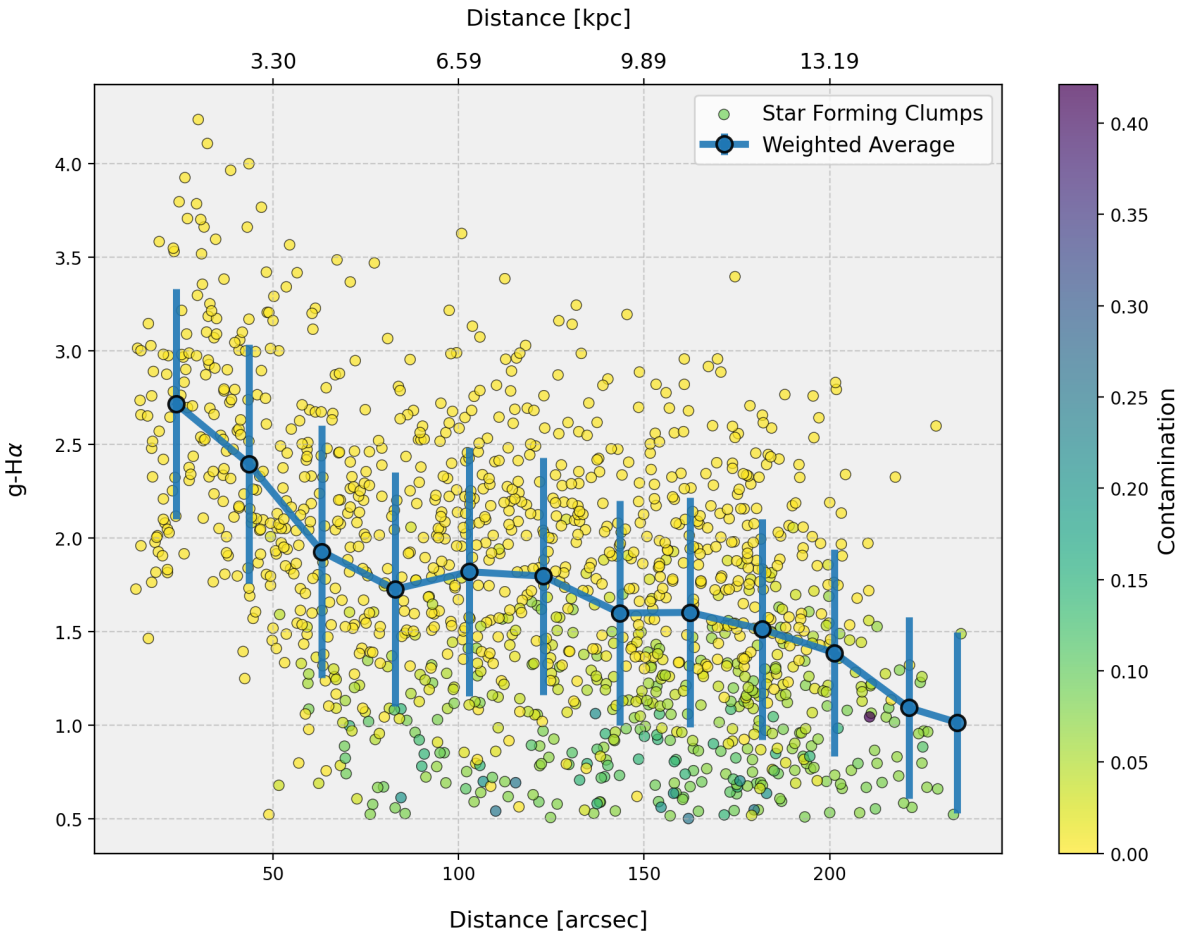

Figure 4.6: NGC 3486 g-Hα color of star-forming clumps as a function of their distance from the galaxy center color coded by contamination. Error bars represent the standard deviation of the weighted average in each distance bin, shown symmetrically in both directions.

Chapter 5

Conclusion

It has been our goal in this study to investigate the star formation processes at the edges of galaxies, focusing on NGC 2712 and NGC 3486. To conduct this study, we used ultra-deep imaging data from the LIGHTS survey in the g and r bands, as well as deep Hα observations from the INT telescope. As a result, we compared the distribution, brightness, and colors of star-forming clumps at the outskirts of galaxies to those in their centers, shedding light on the growth and evolution of galaxy disks.

Before we started this analysis, we discussed several crucial steps, such as data calibration and corrections (G.Golini et al. (2024, in preparation)) , catalog creation (Z.Hosseini-Shahisavandi et al. (2025, in preparation)), and then discussed crucial steps such as prosperity derivation, star-forming clumps selection, and contamination estimation. The study was conducted using catalogs of calibrated images from the g, r, and Hα datasets, ensuring that the continuum had been subtracted from the Hα images. Using Gnuastro tools, other derived properties such as colors and distances from the center of the galaxies have been added to the catalog. We focused on selecting probable star-forming clumps by analyzing their g-Hα color and g-band magnitude and their distance from the center as well in order to understand their ongoing star formation activity.

Based on our findings, star formation at the edges of galaxies differs significantly from that at the centers. We observed that, as the distance from the galaxy center increases, the g-band magnitudes of the star-forming clumps systematically decrease. The trend indicates that star-forming regions on the outskirts are fainter, possibly due to a lower density of stars and a reduced amount of material available.

Moreover, in contrast to the g-Hα color, the g-r color remained relatively uniform across the disk. In fact we observed a clear decrease in g-Hα color with distance, suggesting lower Hα emission as we moved outward. It implies a reduction in ionized gas content as a result of a less efficient star formation process as radii grow larger.

As part of our analysis, we calculated contamination estimates using a 2D histogram from masked field images to account for potential contamination from background or foreground sources. As a result of considering contamination levels and plotting the properties of clumps from masked regions, we were able to further assess the reliability of our clump selections.

These findings have significant implications for the understanding of the current rate of disk growth in galaxies. The observed decrease in star formation activity and intensity as distance increases from the center, may indicate that the outer regions have a less dense environment with less gas availability, resulting in a quiescent star formation phase.

In future work, we plan to estimate the star formation rates of the clumps while accounting for the effects of dust, providing a clearer understanding of the star formation activity in these regions.

Observations of further wavelengths, such as UV or IR, may also shed light on star formation and dust content in low-density regions of the galaxy, enabling a more comprehensive analysis. Moreover, studying the effects of tidal interactions, gas dynamics, and external accretion on the evolution of these star-forming regions would enhance our understanding of galaxy disk evolution.

Bibliography

Abadi, M. G., Navarro, J. F., Steinmetz, M., and Eke, V. R. (2003). Simulations of Galaxy Formation in a Λ Cold Dark Matter Universe. II. The Fine Structure of Simulated Galactic Disks. *he Astrophysical Journal*, 597(1):21–34.

Akhlaghi, M. (2019). Carving out the low surface brightness universe with NoiseChisel. *arXiv e-prints*, page arXiv:1909.11230.

Akhlaghi, M. and Ichikawa, T. (2015). Noise-based Detection and Segmentation of Nebulous Objects. *The Astrophysical Journal Supplement Series*, 220(1):1.

Akhlaghi, M. and Ichikawa, T. (2015). Noise-based detection and segmentation of nebulous objects. *The Astrophysical Journal Supplement Series*, 220(1):1.

Alam, S., Albareti, C., Anders, F., and et al. (2015). The Eleventh and Twelfth Data Releases of the Sloan Digital Sky Survey: Final Data from SDSS-III. *The Astrophysical Journal Supplement Series*, 219(1):12.

Alberts, S., Calzetti, D., Dong, H., Johnson, L. C., Dale, D. A., Bianchi, L., Chandar, R., Kennicutt, R. C., Meurer, G. R., Regan, M., and Thilker, D. (2011). The Evolution of Stellar Populations in the Outer Disks of Spiral Galaxies. *The Astrophysical Journal*, 731(1):28.

Annuar, A., Alexander, D. M., Gandhi, P., Lansbury, G. B., Asmus, D., Baloković, M., Ballantyne, D. R., Bauer, F. E., Boorman, P. G., Brandt, W. N., Brightman, M., Chen, C. T. J., Del Moro, A., Farrah, D., Harrison, F. A., Koss, M. J., Lanz, L., Marchesi, S., Masini, A., Nardini, E., Ricci, C., Stern, D., and Zappacosta, L. (2020). NuSTAR observations of four nearby X-ray faint AGNs: low luminosity or heavy obscuration? *Monthly Notices of the Royal Astronomical Society*, 497(1):229–245.

Aumer, M., White, S. D. M., Naab, T., and Scannapieco, C. (2013). Towards a more realistic population of bright spiral galaxies in cosmological simulations. *mnras*, 434(4):3142–3164.

Bacchini, C., Fraternali, F., Iorio, G., and Pezzulli, G. (2019). Volumetric star formation laws of disc galaxies. *aap*, 622:A64.

Baumann, D. (2022). *Cosmology*. Cambridge University Press.

Bernstein, R. A., Freedman, W. L., and Madore, B. F. (2002). The first detections of the extragalactic background light at 3000, 5500, and 8000 å. iii. cosmological implications. *The Astrophysical Journal*, 571(1):107.

Bertin, E. and Arnouts, S. (1996). SExtractor: Software for source extraction. *Astronomy and Astrophysics Supplement Series*, 117:393–404.

Bigiel, F., Leroy, A., Walter, F., Brinks, E., de Blok, W. J. G., Madore, B., and Thornley, M. D. (2008). The Star Formation Law in Nearby Galaxies on Sub-Kpc Scales. *aj*, 136(6):2846–2871.

Bigiel, F., Leroy, A. K., Walter, F., Brinks, E., de Blok, W. J. G., Kramer, C., Rix, H. W., Schruba, A., Schuster, K. F., Usero, A., and Wiesemeyer, H. W. (2011). A Constant Molecular Gas Depletion Time in Nearby Disk Galaxies. *The Astrophysical Journal*, 730(2):L13.

Bland-Hawthorn, J. and Gerhard, O. (2016). The Galaxy in Context: Structural, Kinematic, and Integrated Properties. *Annual Review of Astronomy and Astrophysics*, 54:529–596.

Buat, V. (2002). Star Formation and Dust Extinction in Nearby Star Forming and Starburst Galaxies. *Astrophysics and Space Science*, 281(1):129–130.

da Cunha, E., Eminian, C., Charlot, S., and Blaizot, J. (2010). New insight into the relation between star formation activity and dust content in galaxies. *Monthly Notices of the Royal Astronomical Society*, 403(4):1894–1908.

de los Reyes, M. A. C. and Kennicutt, Robert C., J. (2019). Revisiting the Integrated Star Formation Law. I. Non-starbursting Galaxies. *The Astrophysical Journal*, 872(1):16.

de Vaucouleurs, G. (1961). Structure of the Virgo Cluster of Galaxies. *he Astrophysical Journal Supplement Series*, 6:213.

Draine, B. T. (2003). Interstellar Dust Grains. *Annual Review of Astronomy and Astrophysics*, 41:241–289.

El-Badry, K., Wetzel, A., Geha, M., Hopkins, P. F., Kereš, D., Chan, T. K., and Faucher-Giguère, C.-A. (2016). Breathing FIRE: How Stellar Feedback Drives Radial Migration, Rapid Size Fluctuations, and Population Gradients in Low-mass Galaxies. *The Astrophysical Journal*, 820(2):131.

Elmegreen, B. G. (1997). Theory of Starbursts in Nuclear Rings. In Franco, J., Terlevich, R., and Serrano, A., editors, *Revista Mexicana de Astronomia y Astrofisica Conference Series*, volume 6 of *Revista Mexicana de Astronomia y Astrofisica Conference Series*, page 165.

Elmegreen, B. G. (1997). Theory of starbursts in nuclear rings. In *Revista Mexicana de Astronomia y Astrofisica Serie de Conferencias, Vol. 6, 1st Guillermo Haro Conference on Astrophysics: Starburst Activity in Galaxies, Puebla, Pue., Mexico, April 29-May 3, 1996, p. 165.*, volume 6, page 165.

Erwin, P. (2004). Double-barred galaxies. I. A catalog of barred galaxies with stellar secondary bars and inner disks. *The Astrophysical Journal*, 415:941–957.

Eskandarlou, S., Akhlaghi, M., Infante-Sainz, R., Saremi, E., Raji, S., Sharbaf, Z., Golini, G., Ghaffari, Z., and Knapen, J. H. (2023). Gnuastro: Estimating the Zero-point Magnitude in Astronomical Imaging. *Research Notes of the American Astronomical Society*, 7(12):269.

Foschini, L., Di Cocco, G., Dadina, M., Bassani, L., Cappi, M., Stephen, J. B., Trifoglio, M., Gianotti, F., Ho, L. C., Mulchaey, J., Panessa, F., and Piconcelli, E. (2002). First Results from a XMM-Newton Survey of a Distance-Limited (D ¡ 22 Mpc) Sample of Seyfert Galaxies. II - The Galactic Serendipitous Sources. *arXiv e-prints*, pages astro–ph/0202247.

Gao, Y. and Solomon, P. M. (2004). The Star Formation Rate and Dense Molecular Gas in Galaxies. *The Astrophysical Journal*, 606(1):271–290.

Haydon, D. T., Kruijssen, J. M. D., Chevance, M., Hygate, A. P. S., Krumholz, M. R., Schruba, A., and Longmore, S. N. (2020). An uncertainty principle for star formation - III. The characteristic emission time-scales of star formation rate tracers. *mnras*, 498(1):235–257.

Heavens, A. (2008). The cosmological model: an overview and an outlook. *Journal of Physics: Conference Series*.

Hill, J. M., Green, R. F., Ashby, D. S., Brynnel, J. G., Cushing, N. J., Little, J. K., Slagle, J. H., and Wagner, R. M. (2012). The Large Binocular Telescope. In Stepp, L. M., Gilmozzi, R., and Hall, H. J., editors, *Ground-based and Airborne Telescopes IV*, volume 8444 of *Society of Photo-Optical Instrumentation Engineers (SPIE) Conference Series*, page 84441A.

Hodge, P. W. (1983). The Hubble type of the Milky Way Galaxy. *Publications of the Astronomical Society of the Pacific*, 95:721–723.

Houjun Mo, F. V. D. B. and White, S. (2010). Galaxy Formation and Evolution. *United States of America by Cambridge University Press, New York*.

Huchtmeier, W. K. and Richter, O. G. (1985). HI-observations of isolated spiral galaxies. *The Astrophysical Journal*, 149:118–122.

Ivezić, Ž., Lupton, R. H., Schlegel, D., Boroski, B., Adelman-McCarthy, J., Yanny, B., Kent, S., Stoughton, C., Finkbeiner, D., Padmanabhan, N., Rockosi, C. M., Gunn, J. E., Knapp, G. R., Strauss, M. A., Richards, G. T., Eisenstein, D., Nicinski, T., Kleinman, S. J., Krzesinski, J., Newman, P. R., Snedden, S., Thakar, A. R., Szalay, A., Munn, J. A., Smith, J. A., Tucker, D., and Lee, B. C. (2004). SDSS data management and photometric quality assessment. *Astronomische Nachrichten*, 325(6):583–589.

Kennicutt, R. C., J. (2001). Stellar Structure of the Galaxy: Overview. In Woodward, C. E., Bicay, M. D., and Shull, J. M., editors, *Tetons 4: Galactic Structure, Stars and the Interstellar Medium*, volume 231 of *Astronomical Society of the Pacific Conference Series*, page 2.

Kennicutt, Robert C., J. (1989). The Star Formation Law in Galactic Disks. *The Astrophysical Journal*, 344:685.

Kennicutt, R. C. and Evans, N. J. (2012). Star Formation in the Milky Way and Nearby Galaxies. *Annual Review of Astronomy and Astrophysics*, 50:531–608.

Kennicutt Jr, R. C. (1998). The global schmidt law in star-forming galaxies. *The astrophysical journal*, 498(2):541.

Khoperskov, A. V., Moiseev, A. V., and Chulanova, E. A. (2001). Dynamical modeling of SB galaxies. *Bulletin of the Special Astrophysics Observatory*, 52:134–144.

Krumholz, M. R., Dekel, A., and McKee, C. F. (2011). A universal, local star formation law in galactic clouds, nearby galaxies, high-redshift disks, and starbursts. *The Astrophysical Journal*, 745(1):69.

Krumm, N. and Shane, W. W. (1982). Neutral hydrogen in two extremely isolated galaxies. *The Astrophysical Journal*, 116:237–247.

Lada, C. J., Forbrich, J., Lombardi, M., and Alves, J. F. (2012). Star Formation Rates in Molecular Clouds and the Nature of the Extragalactic Scaling Relations. *The Astrophysical Journal*, 745(2):190.

Lianou, S., Barmby, P., Mosenkov, A. A., Lehnert, M., and Karczewski, O. (2019). Dust properties and star formation of approximately a thousand local galaxies. *Astronomy and Astrophysics*, 631:A38.

Madau, P. and Dickinson, M. (2014). Cosmic star-formation history. *Annual Review of Astronomy and Astrophysics*, 52(1):415–486.

Márquez, I., Durret, F., Delgado, R. G., Marrero, I., Masegosa, J., Maza, J., Moles, M., Perez, E., and Roth, M. (1999). Near-infrared photometry of isolated spirals with and without an agn-i. the data. *Astronomy and Astrophysics Supplement Series*, 140(1):1–14.

McKee, C. F. and Ostriker, E. C. (2007). Theory of star formation. *Annu. Rev. Astron. Astrophys.*, 45(1):565–687.

Moustakas, J., Lang, D., Dey, A., Juneau, S., Meisner, A., Myers, A. D., Schlafly, E. F., Schlegel, D. J., Valdes, F., Weaver, B. A., and Zhou, R. (2023). Siena Galaxy Atlas 2020. *apjs*, 269(1):3.

Ostriker, E. C. and Shetty, R. (2011). Maximally star-forming galactic disks. i. starburst regulation via feedback-driven turbulence. *The Astrophysical Journal*, 731(1):41.

Pedichini, F. and Speziali, R. (2004). The Optimized Cryostat for the LBC Camera. In Amico, P., Beletic, J. W., and Belectic, J. E., editors, *Scientific Detectors for Astronomy, The Beginning of a New Era*, volume 300 of *Astrophysics and Space Science Library*, pages 349–366.

Ragazzoni, R., Giallongo, E., Pasian, F., Pedichini, F., Fontana, A., Marconi, G., Speziali, R., Turatto, M., Danziger, J., Cremonese, G., Smareglia, R., Gallieni, D., Anaclerio, E., and Lazzarini, P. G. (2000). Double prime focus camera for the F/1.14 Large Binocular Telescope. In Iye, M. and Moorwood, A. F., editors, *Optical and IR Telescope Instrumentation and Detectors*, volume 4008 of *Society of Photo-Optical Instrumentation Engineers (SPIE) Conference Series*, pages 439–446.

Saintonge, A., Kauffmann, G., Wang, J., Kramer, C., Tacconi, L. J., Buchbender, C., Catinella, B., Graciá-Carpio, J., Cortese, L., Fabello, S., Fu, J., Genzel, R., Giovanelli, R., Guo, Q., Haynes, M. P., Heckman, T. M., Krumholz, M. R., Lemonias, J., Li, C., Moran, S., Rodriguez-Fernandez, N., Schiminovich, D., Schuster, K., and Sievers, A. (2011). COLD GASS, an IRAM legacy survey of molecular gas in massive galaxies - II. The non-universality of the molecular gas depletion time-scale. *mnras*, 415(1):61–76.

Sandage, A. and Tammann, G. A. (1981). *A Revised Shapley-Ames Catalog of Bright Galaxies*. Washington: Carnegie Institution.

Schlegel, D. J., Finkbeiner, D. P., and Davis, M. (1998). Maps of Dust Infrared Emission for Use in Estimation of Reddening and Cosmic Microwave Background Radiation Foregrounds. *The Astrophysical Journal*, 500(2):525–553.

Schmidt, M. (1959a). The Rate of Star Formation. *The Astrophysical Journal*, 129:243.

Schmidt, M. (1959b). The Rate of Star Formation. *The Astrophysical Journal*, 129:243.

Sellwood, J. A. and Binney, J. J. (2002). Radial mixing in galactic discs. *mnras*, 336(3):785–796.

Shen, J. and Zheng, X.-W. (2020). The bar and spiral arms in the Milky Way: structure and kinematics. *Research in Astronomy and Astrophysics*, 20(10):159.

Shivaei, I., Reddy, N. A., Steidel, C. C., and Shapley, A. E. (2015). Investigating Hα, UV, and IR Star-formation Rate Diagnostics for a Large Sample of z $\sim$ 2 Galaxies. *The Astrophysical Journal*, 804(2):149.

Trujillo, I., D'Onofrio, M., Zaritsky, D., Madrigal-Aguado, A., Chamba, N., Golini, G., Akhlaghi, M., Sharbaf, Z., Infante-Sainz, R., Román, J., Morales-Socorro, C., Sand, D., and Martin, G. (2021). Introducing the lbt imaging of galactic halos and tidal structures (lights) survey. a preview of the low surface brightness universe to be unveiled by lsst. *Astronomy & Astrophysics*, 654.

Trujillo, I. and Fliri, J. (2016). Beyond 31 mag arcsec^{-2}: The Frontier of Low Surface Brightness Imaging with the Largest Optical Telescopes. *The Astrophysical Journal*, 823(2):123.

Weisz, D. R., Johnson, B. D., Johnson, L. C., Skillman, E. D., Lee, J. C., Kennicutt, R. C., Calzetti, D., van Zee, L., Bothwell, M. S., Dalcanton, J. J., Dale, D. A., and Williams, B. F. (2012). Modeling the Effects of Star Formation Histories on Hα and Ultraviolet Fluxes in nearby Dwarf Galaxies. *The Astrophysical Journal*, 744(1):44.

Wong, T. and Blitz, L. (2002). The Relationship between Gas Content and Star Formation in Molecule-rich Spiral Galaxies. *The Astrophysical Journal*, 569(1):157–183.

Zaritsky, D., Golini, G., Donnerstein, R., Trujillo, I., Akhlaghi, M., Chamba, N., D'Onofrio, M., Eskandarlou, S., Zahra Hosseini-ShahiSavandi, S., Infante-Sainz, R., Martin, G., Montes, M., Román, J., Sedighi, N., and Sharbaf, Z. (2024). LIGHTS. Survey Overview and a Search for Low Surface Brightness Satellite Galaxies. *arXiv e-prints*, page arXiv:2406.01912.

Aknowledgement

This thesis would not have been possible without the invaluable guidance of my supervisor, Prof. Mauro D'onofrio, and my co-supervisor, Prof. Ignacio Trujillo. I appreciated the expertise and insight provided by Professor D'Onofrio, who guided the overall direction of this work and motivated me to think critically about each challenge. On the other hand, Professor Trujillo (Nacho)'s meticulous feedback and constant help refined my approach and enabled me to understand the implications of my research. The combined mentorship of both of them has greatly contributed to the development of this thesis and has made the journey both enjoyable and rewarding.

The special thanks goes to Zahra Hosseini Shahsavandi, my colleague, collaborator, and motivator. At every turn, her tireless support and willingness to brainstorm have been invaluable. It is always a pleasure to have you on my side.

I am also grateful to the incredible group I was fortunate to be part of each week. In addition to providing me with fresh perspectives, discussing our work together also motivated me during challenging times.

Thank you for supporting me; Mom, Dad, and my brother Bobak, you are the reason I have made it this far. Having your love and belief in me is my foundation and my driving force.

To Aidin, my partner, thank you for being my rock and my constant source of strength that made this journey much lighter.

Finally, to the wonderful friends in my life, Zahra, Farid, Golnar, Hanie and Mina. You filled this time filled with laughter, perspective, and endless support. The journey has been made meaningful by each of them, which has made it more than just about research.